

# Journal of Geophysical Research: Solid Earth

## RESEARCH ARTICLE

10.1029/2018JB016214

**Key Points:**

- We perform Earthquake rupture dynamics using slip weakening friction in 2-D to calculate stress and slip in the off-fault material
- We calculate the Coulomb stress change on the receiver faults, based on the static stresses changes in the off-fault material
- We consider the main fault to be rough, where roughness is defined through self-affine fractality

**Supporting Information:**

- Supporting Information S1

**Correspondence to:**

K. S. Aslam,  
ksaslam@memphis.edu

**Citation:**

Aslam K. S., & Daub, E. G. (2018). Effect of fault roughness on aftershock distribution: Elastic off-fault material properties. *Journal of Geophysical Research: Solid Earth*, 123. <https://doi.org/10.1029/2018JB016214>

Received 13 JUN 2018

Accepted 25 SEP 2018

Accepted article online 30 SEP 2018

## Effect of Fault Roughness on Aftershock Distribution: Elastic Off-Fault Material Properties

**Khurram S. Aslam<sup>1</sup>  and Eric G. Daub<sup>1</sup> **<sup>1</sup>Center for Earthquake Research and Information, University of Memphis, Memphis, TN, USA

**Abstract** We perform physics-based simulations of earthquake rupture propagation on geometrically complex strike-slip faults to examine the off-fault stress changes resulting from dynamic fault slip. We consider many different realizations of the fault profile and use the output of our simulations to calculate the Coulomb failure function (CFF) for each realization. We analyze the effects of fault maturity as well as the self-affine character of the fault surface on the stress field. To quantify our results, we calculate the probability density function for the CFF as a function of distance and observe that the CFF values show a greater variability in the near-fault region (distance  $<3$  km away from fault), and this spread squeezes into a narrow negative range in the far-field region. In the near-fault region, we see many zones of positive CFF change, which are not observed in the far-fault region. We consider these zones of CFF increase as locations of potential aftershocks and compare their size with rupture areas of aftershocks from relocated earthquake catalogs of Northern and Southern California. Our model results and observational data show a relatively high probability of occurrence of smaller potential aftershock areas compared to larger ones in the near-fault region. Additionally, based on our comparison with aftershock and preshock data, we conclude that the stresses in the near-fault region are dominated by fault roughness effects. Our results suggest that tectonic stresses are highly spatially heterogeneous, and this complexity persists throughout seismic cycle.

### 1. Introduction

The triggering mechanism of aftershocks is an aspect of earthquake occurrence, which is not fully understood. Many authors have proposed different effects such as static stress changes (King et al., 1994), passing seismic wave-induced dynamic stresses (Gomberg et al., 2003; Hill et al., 1993), afterslip (Perfettini & Avouac, 2004), fluid flow (Nur & Booker, 1972), static stress triggering of rate-and-state nucleation sites (Dieterich, 1994), and the evolution of viscoelastic damage rheology (Ben-Zion & Lyakhovsky, 2006). All of these effects are believed to play a role in aftershock triggering, but the exact contribution of each mechanism is not known. Another factor complicating the identification of causative effect of aftershock triggering is the delay in time of the aftershock events relative to the main shock. Because of these observational challenges, it is not always possible to identify the specific physics at work. While static stress changes explain many features of aftershocks, one shortcoming of this model is that it cannot explain aftershock occurrence in stress shadows. As an example, the  $M_w = 6.9$  1989 Loma Prieta Earthquake has many aftershocks occurring in regions of stress increase but there are additional aftershocks which occurred in the regions of stress shadows (Segou & Parsons, 2014). Furthermore, focal mechanisms following the Loma Prieta event are diverse and are not aligned with the directions expected for static stress triggering (Beroza & Zoback, 1993; Kilb et al., 1997).

In order to better understand aftershock triggering by static stresses, we perform earthquake rupture simulations on rough faults and use physical models of slip and stress to estimate the expected aftershock locations following a large earthquake. Dynamic rupture simulations calculate fault slip by combining elastic wave propagation with fault constitutive laws to generate a spontaneous physics-based model of faulting. This modeling resolves the finer scale details of slip based on elasticity and friction and hence has the ability to predict the spatial distribution of slip and stress changes, features that are not resolved by stress changes estimated using observational data (Freed, 2005). Dynamic rupture simulations have been widely used to infer information related to physical processes occurring during rupture propagation (Aochi et al., 2000; Bazzani & Cocco, 2005; Dalguer et al., 2003; Daub & Carlson, 2008; Daub et al., 2010; Dunham & Archuleta, 2005; Harris, 2004; Harris & Day, 1997; Shi & Ben-Zion, 2006; Shi & Day, 2013; Tinti et al., 2005).

Real faults exhibit complex geometries and these geometrical complexities introduce heterogeneities in the stress distribution when the fault slips (Brown & Scholz, 1985; Candela et al., 2012; Power et al., 1987; Power & Tullis, 1995; Renard et al., 2006). Studies have shown that during fault slip, nonplanar fault geometry can introduce normal and shear stress perturbations that are in many cases comparable to the prevailing stresses (Chester & Chester, 2000; Dieterich & Smith, 2009). Many simulation studies (dynamic rupture propagation as well as earthquake ground motions) have been performed considering faults as rough surfaces to examine how rupture propagates on rough faults in comparison to flat faults and how the surface ground motions at high or low frequency vary as a result of earthquake nucleation and propagation on complex faults. Dieterich and Smith (2009) studied the interactions among slip and off-fault stressing during slip on rough faults by assuming quasi-static slip on the fault with a constant frictional coefficient. They observed that linear scaling of fault slip with fault length is no longer observed for faults showing realistic roughness values observed for natural faults. A study by Dunham et al. (2011a) showed that dynamic ruptures on rough faults produce accelerograms exhibiting similar characteristics at high frequencies to those observed in strong motion records from real earthquakes. Fang and Dunham (2013) studied the effect of fault roughness to observe the influence of supplementary tractions introduced on the fault due to its roughness. They related differences in the observed background stress level required to generate moderate to large earthquakes for mature and immature faults to an effective additional shear resistance termed *roughness drag* due solely to fault roughness. Bruhat et al. (2016) also explored the behavior of rupture propagation on rough faults and observed that supershear rupture transitions are more likely to be seen on rougher faults as compared to flat faults. Based on investigation of some special cases, they related those that favored transition to rupture propagation into a segment that is unfavorably oriented, or to rupture deceleration due to an unfavorable bend. They further observed that sustained propagation of these supershear ruptures occur mostly on fault sections that are smoother than average. Shi and Day (2013) performed dynamic rupture and ground motion simulations in three dimensions (3-D) on rough faults and observed that local stress perturbations due to nonplanarity cause incoherence in the rupture process and found that the ground-motion intensities estimated from their simulations are statistically similar to those of ground motion prediction equations.

In this study, we build upon these previous studies and carry out a suite of two-dimensional (2-D) simulations of earthquakes on strike slip faults exhibiting complex geometry to fully quantify the stress change resulting from dynamic slip on the fault. Since real faults are represented by self affine fractals (Candela et al., 2012), we consider a range of fault roughness parameters representing major faults and run simulations with numerous realizations of each set of fault roughness parameter values. We calculate the Coulomb failure function (CFF) for each of these realizations and quantify the CFF by computing its probability density function (PDF). We compare our model predictions with observations of aftershock distributions in space using relocated earthquake catalogs of Northern and Southern California (Shearer et al., 2005; Waldhauser & Schaff, 2008). Since the main emphasis of this work is to observe how the heterogeneous stress distribution associated with the fault roughness can be related to the aftershock distribution, we analyze the seismicity both before and after major earthquakes. Doing this helps us distinguish the effects of heterogeneous stress distribution caused by fault roughness on stresses present in the off-fault region during the preseismic phase and new stresses imposed in the same region during the postseismic phase.

## 2. Model Setup

### 2.1. Fault Roughness

A fault appears as linear feature on the surface of earth with wavy irregularities (Brown & Scholz, 1985; Candela et al., 2012). These irregularities are observed at all scales that have been measured (Brown & Scholz, 1985; Power et al., 1987; Power & Tullis, 1995; Renard et al., 2006). A newly fractured rock shows a fractal profile, and then subsequent slip decreases the amplitude of the roughness while still maintaining its fractal characteristics (Sagy et al., 2007). Figure 1a shows the roughness of a fault profile in the direction parallel to the slip of the fault. Self-similar and self-affine fractal fault profiles are commonly used to describe observed fault roughness. The detailed description of these types of fault profiles can be found in Appendix A.

In this study, we use two parameters to describe fault roughness. The first parameter is the Hurst exponent and the second parameter is the root-mean-square (RMS) height to wavelength ratio. A detailed description of these parameters can be found in Appendix A. We simulate earthquake rupture propagation on self-affine faults with 100 different realizations of the fault profile for each choice of  $H$  and RMS height. For each realization of fault roughness, the parameters are taken from observational values of real faults, that is,  $H$  ranging

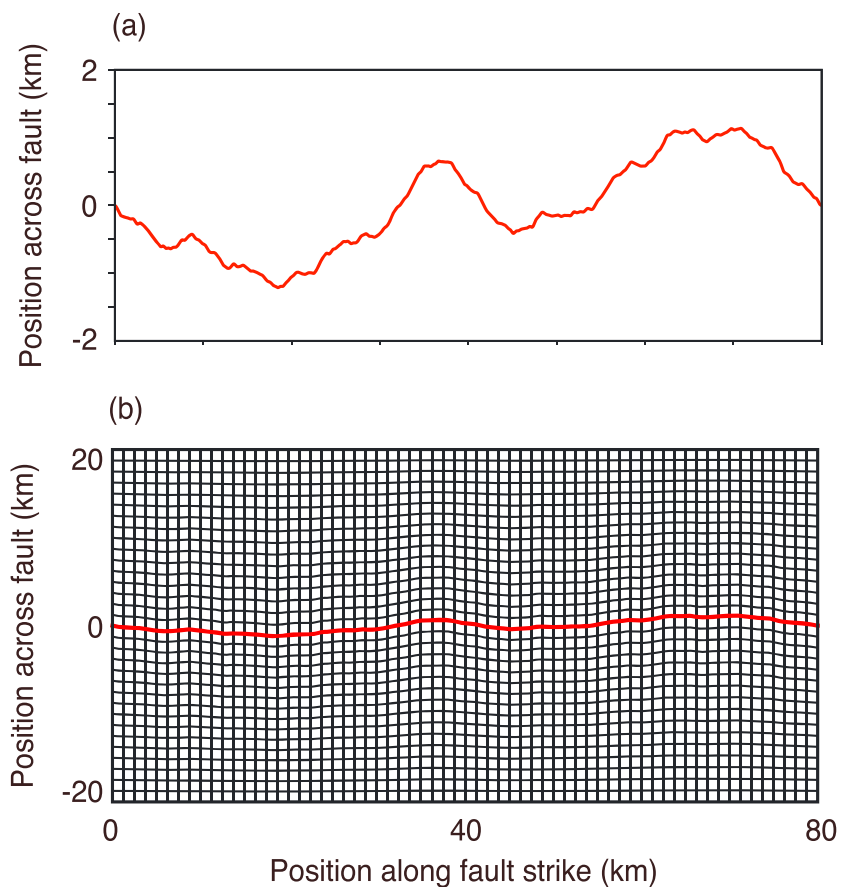


**Figure 1.** Modeling setup of our simulations of slip on a rough strike-slip fault. (a) Fault roughness profile is shown with root-mean-square height to wavelength ratio of 0.01 and Hurst exponent of 1.0. The minimum wavelength of the profile is 500 m. The fault profile is vertically exaggerated. (b) Domain setup of the fault trace shown in (a), shown to scale. The fault profile is shown in red color. The grid is constructed using transfinite interpolation. We perform 100 simulations of each combination of roughness parameter, but in each case, the domain dimensions remain the same, 80 km long and 40 km wide. In each simulation, the fault profile is different, which in turn changes the grid to be used for solving the rupture propagation problem using finite differences.

from 0.6 to 1 and RMS height to wavelength ratio of  $10^{-2}$  and  $10^{-3}$ . A Fourier method is used to generate the fault surface with the desired spectrum and random phase (Andrews & Barall, 2011) with zero mean. Due to the finite numerical resolution of our simulations, we cut off the fractal at a minimum wavelength corresponding to 20 times the grid spacing to ensure that our modeling is well resolved.

## 2.2. Dynamic Rupture Model

We consider a 2-D plane strain model for simulation of dynamic rupture propagation as seen in Figure 1 (b). The domain is 80 km long and 40 km wide. The fault surface is given by the curve  $f(x)$  which deviates from  $y = 0$  based on the values of Hurst exponent and RMS height to wavelength ratio. For each combination of fault roughness parameters, we run simulations of rupture propagation for 100 different realizations of the fault surface. We run all our simulations with a grid spacing  $\Delta x = 25$  m. We have also run a few additional simulations with a smaller grid spacing ( $\Delta x = 10$  and 5 m) to confirm that our simulations are well resolved at  $\Delta x = 25$  m. The selected  $\Delta x$  gives a resolvable (minimum) fault roughness wavelength  $\lambda_{min} = 20 \Delta = 500$  m = 0.5 km for all of our simulations. We use rupture dynamics code `fdfault`, which solves the elastodynamic wave equation using finite differences and has been verified against multiple benchmark problems of the SCEC/USGS rupture code verification group (Harris et al., 2009; Harris et al., 2018). We run our simulations to 4th order accuracy in both space and time. Fault and external boundary conditions are imposed weakly (Kozdon et al., 2012), resulting in a method that is globally fourth order accurate (Kozdon et al., 2013). The code handles the irregular geometry of the fault surface through algebraic coordinate transformations on a structured grid (Liseikin, 2009).

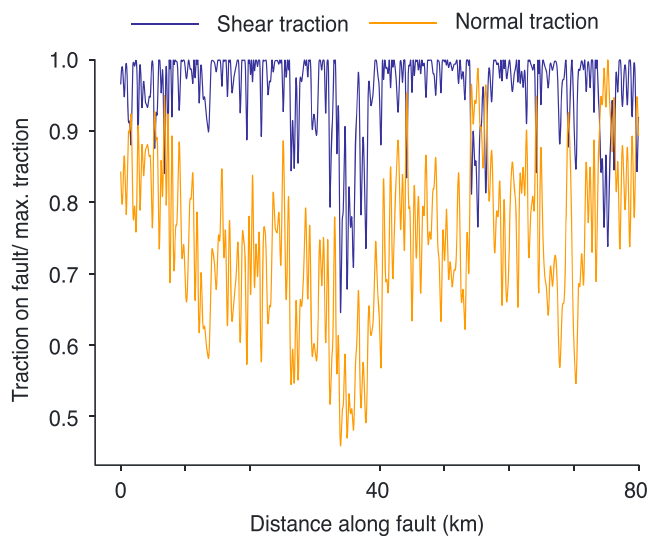


**Figure 2.** Normal and shear tractions resolved on the fault plane. The fault roughness causes the tractions to be highly heterogeneous along the fault even if the regional stresses are uniform across the whole domain.

We assume a uniform initial background stress field (negative in compression) in all of our simulations. Because of the varied fault profile, the uniform stress tensor leads to heterogeneous initial shear and normal tractions along the fault. Figure 2 shows the normalized values of shear and normal traction resolved on each point on the fault plane from the uniform regional stress tensor. As can be seen in Figure 2, the traction values are highly heterogeneous, with values as low as half of the maximum value of traction. Depending on the realization of the fault surface, some ruptures may arrest at a geometrically unfavorable bend and die out early, so to avoid this, we choose initial background stress field values (given in Table 1) that ensure at least 90% of ruptures propagate 50 km from the nucleation point before dying out.

**Table 1**  
*List of Parameter Values Used in This Study*

	Parameter name	Symbol used	Value
Model domain parameters			
	Domain length	$X_{tot}$	80 km
	Domain width	$Y_{tot}$	40 km
Material properties parameters			
	Shear wave speed	$\alpha$	6,000 m/s
	Compressional wave speed	$\beta$	3,464 m/s
	Lame's parameters	$\lambda$ and $G$	32.04 GPa
Friction law parameters			
	Static frictional coefficient	$\mu_s$	0.7
	Dynamic frictional coefficient	$\mu_d$	0.2
	Critical slip distance	$D_c$	0.4 m
Initial condition parameters			
	Stress	$\sigma_{xx}$	-100 MPa
	Stress	$\sigma_{xy}$	45 MPa
	Stress	$\sigma_{yy}$	-110 MPa
Fault roughness parameters			
	Hurst exponent	$H$	0.6–1.0
	RMS height to wavelength ratio	$\gamma$	0.01, 0.001

Note. RMS = root-mean-square.

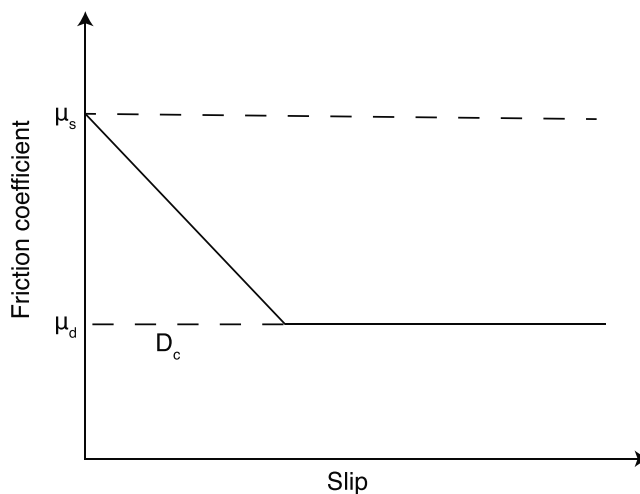


**Figure 3.** Friction on the fault is governed by the linear slip weakening law. No slip occurs until the ratio of shear to normal stress reaches the static friction  $\mu_s$ . Once slip initiates, the friction decreases linearly with slip to the dynamic coefficient  $\mu_d$  over a critical slip distance  $D_c$ .

We model the friction on the fault using the linear slip weakening (SW) friction law (Andrews, 1976, 1985; Day, 1982; Ida, 1972). This friction law has been widely adopted in dynamic rupture simulations (Harris et al., 2009) and is conceptually simpler in implementation (Bizzarri, 2010) when compared to other friction laws such as rate and state friction (Dieterich, 1979; Ruina, 1983) or the Shear Transformation Zone friction law (Daub & Carlson, 2010). For the SW law, the friction on the fault  $\mu$  is a function of the slip  $U$  on the fault. The initial friction on the fault  $\mu_s$  drops to a dynamic friction value  $\mu_d$  over a critical slip distance  $D_c$  as a function of slip:

$$\mu(U) = \begin{cases} (\mu_s - \mu_d)(1 - \frac{U}{D_c}) + \mu_d & \text{for } U < D_c \\ \mu_d & \text{for } U \geq D_c \end{cases} \quad (1)$$

Figure 3 illustrates the slip-dependent friction coefficient, where the friction linearly drops from static friction to dynamic friction over a critical distance given by  $D_c$ . We choose  $D_c = 0.4$  m,  $\mu_s = 0.7$  and  $\mu_d = 0.2$  in all of our simulations. The low dynamic friction is chosen based on lab experiments that show strong dynamic weakening at co-seismic slip speeds (Beeler et al., 2008; Di Toro et al., 2004; Di Toro et al., 2011; Goldsby & Tullis, 2011, 2002; Hirose & Bystricky, 2007; Hirose & Shimamoto, 2005; Tsutsumi & Shimamoto, 1997). A complete list of parameter values used in this study is given in Table 1.

It is important to note that the friction on the fault is also spatially variable due to the heterogeneous distribution of slip, and each point on the fault fails individually based on the stress changes from wave propagation and fault slip. In some of our simulations, we also encounter tensile normal traction at some points on the fault during fault slip. We do not allow fault opening in these simulations, and set the fault to have zero shear strength when tensile normal tractions occur.

In all of our simulations, we start rupture near the center of the fault. We also vary our rupture nucleation strategy for a single realization of each fault profile to ensure that our results do not depend on the nucleation method. After examining the results from each nucleation method, we default to the simplest strategy of a statically overstressed nucleation patch for our full set of simulations. The details of the rupture nucleation strategies that we consider can be found in Appendix B.

### 2.3. CFF and Synthetic Aftershock Calculations

Our dynamic rupture simulations calculate the change in stresses throughout the history of the dynamic rupture, and thus, we directly obtain the full stress tensor after the earthquake from our simulation output. Using the stress tensor we calculate the CFF using the method given in Appendix C. For all of our CFF calculations, we choose the orientations of receiver faults to be parallel to the overall trace of the main fault. As we are interested in calculating the static stress changes from our simulation results, we do not want the final stresses to include the effects of dynamic wave propagation. To ensure this, we choose a smaller portion of the domain (40 km along the fault and 30 km across the fault) and extract the stress tensor in all of our calculations after the dynamic waves have had sufficient time to propagate away from the central portion of the domain. Since our selected shear wave velocity is 3.464 km/s, we allow 18.4 s to give the waves sufficient time to propagate across the entire domain, and away from the central region. To ensure that the point statistics of CFF in the portion of the domain used for analysis are not affected by boundary effects, we run a few additional simulations with a larger domain size. We find that the results presented here are independent of the computational domain size.

In addition to point statistics of the CFF, we also analyze its spatial correlations. In particular, we are interested in the spatial dimension of these correlations. Using the CFF calculations for all 100 realizations of fault profile, we count the zones of positive CFF surrounding the main fault and quantify their size and distance from the fault. Based on the minimum roughness wavelength of the fault profiles, we only consider those positive CFF zones that are at least 500 m long. Our goal is to determine if potential aftershock zones follow any particular spatial trend as a function of distance from the fault. We also compare the spatial correlations in our modeling results with real aftershock observations to make quantitative comparisons. This comparison can further help us examine if there is any relationship between aftershock size, location, and fault roughness. To describe

the process of calculating positive CFF zone area in detail, we first select a region of positive CFF at a random distance away from the main fault and calculate its length following the strike of the main fault. This length is then converted into rupture area by supposing that the positive CFF zone hosts a circular patch rupture at that distance. The idea that small to moderate magnitude earthquake ruptures have a circular dimension is supported by previous work showing the stress drop is independent of source dimensions (Aki, 1972; Allmann & Shearer, 2009; Hanks, 1977; Scholz, 1982; Thatcher & Hanks, 1973). The rupture area then indicates the maximum area that can be ruptured by a hypothetical aftershock at that particular location. We calculate this maximum possible rupture area for each positive CFF zone at each distance for all realizations of fault surface so that we have a statistical ensemble for many different ruptures.

### 3. Results

Figure 4 shows the change in (a) normal and (b) shear stress in a rectangular area extending from 20 to 60 km along the fault and from –15 to 15 km across the fault. As seen in the plot, the stresses are spatially heterogeneous but the negative stresses can be seen to dominate the modeling domain, particularly for locations not in the immediate vicinity of the fault surface. We refer to the area near the fault where stresses are highly heterogeneous as the *near-fault* region, while we term the more distant region where stresses are more uniform the *far-fault* region. However, we note that though both of these regions are very close to the fault when viewed on a tectonic scale. The extent of these regions is shown in Figure 5. We focus our discussion on the *near-fault* region, as it is the region where the fault roughness effects are dominant. The magnitude of the stress fluctuations decrease as the distance from the fault increases and we note that more uniformity in the stress change is observed at greater distances.

In Figure 4, we find that zones near the hypocenter exhibit larger stress changes than the changes that are observed for sections into which the rupture has propagated. This behavior is observed in all of our simulations. The presence of these zones is related to the nucleation procedure used to start the dynamic rupture. In the case of Figure 4, the rupture was initiated at a point 39 km along fault distance with a width of 3 km as is noted in Figure 4.

After extracting shear and normal stresses for all of our simulations, we calculate the CFF on receiver faults near the main fault with orientations parallel to the trace of the main fault. Using stresses from Figure 4, the calculated CFF change is shown in Figure 5a for the same fault realization. The CFF is highly heterogeneous with positive and negative CFF changes visible around the fault. The negative CFF change values dominate the far-fault region, while mixed positive and negative CFF values dominate the near-fault region. It is important to observe that there are many lobes of positive CFF change in the near-fault region due to roughness of the fault profile. Three of these lobes are labeled on Figure 5 with A, B, and C. These positive CFF lobes are potential sources of aftershocks, particularly since the areas where they appear would be seen as stress shadows in typical static stress change calculations due to insufficient resolution of the fault slip. At far-fault distances, negative CFF zones dominate, since the fault roughness effects are not present in the far-fault regions.

Since we calculate the CFF for each individual fault realization, we estimate the width of the near-fault region on each side of the fault in each realization. We do this by calculating the maximum distance away from the fault with more than five positive CFF zones. We do not see any significant variation of the near-fault region width with the value of  $H$ . This is evident from Figure 5 where the width of the near-fault region for  $H = 1$  and  $H = 0.6$  is shown for RMS ratio of 0.01. We find that the width of the near-fault region changes with the RMS ratio of the fault roughness. Decreasing the RMS ratio from 0.01 to 0.001, we see a decrease in the width of the near-fault region. Using the simulation results, we can calculate the average width of the near-fault region over all of our realizations. The average width of the near-fault region on either side of the fault is  $\sim 2.7$  km for fault profiles having RMS height of 0.01 and  $\sim 0.9$  km for faults having RMS height of 0.001. For distances greater than this width, we observe fewer than five zones with positive CFF. In the far-field, the CFF function is always negative; thus there is an intermediate region with between one and five zones of positive CFF. This region starts where the near-fault region ends and reaches to a maximum distance of  $\sim 5.5$  km away from fault for the case of RMS of 0.01. Points beyond the intermediate region are part of the far-fault region.

We examine the statistical properties of the change in static stresses by combining the results for all 100 realizations for each value of  $H$  and the RMS height. For computing the CFF function, we only consider those ruptures that have propagated at least 50 km. We see that under our given set of initial conditions (Table 1), all the ruptures with a fault profile having RMS height of 0.001 reach this distance and for fault profiles with

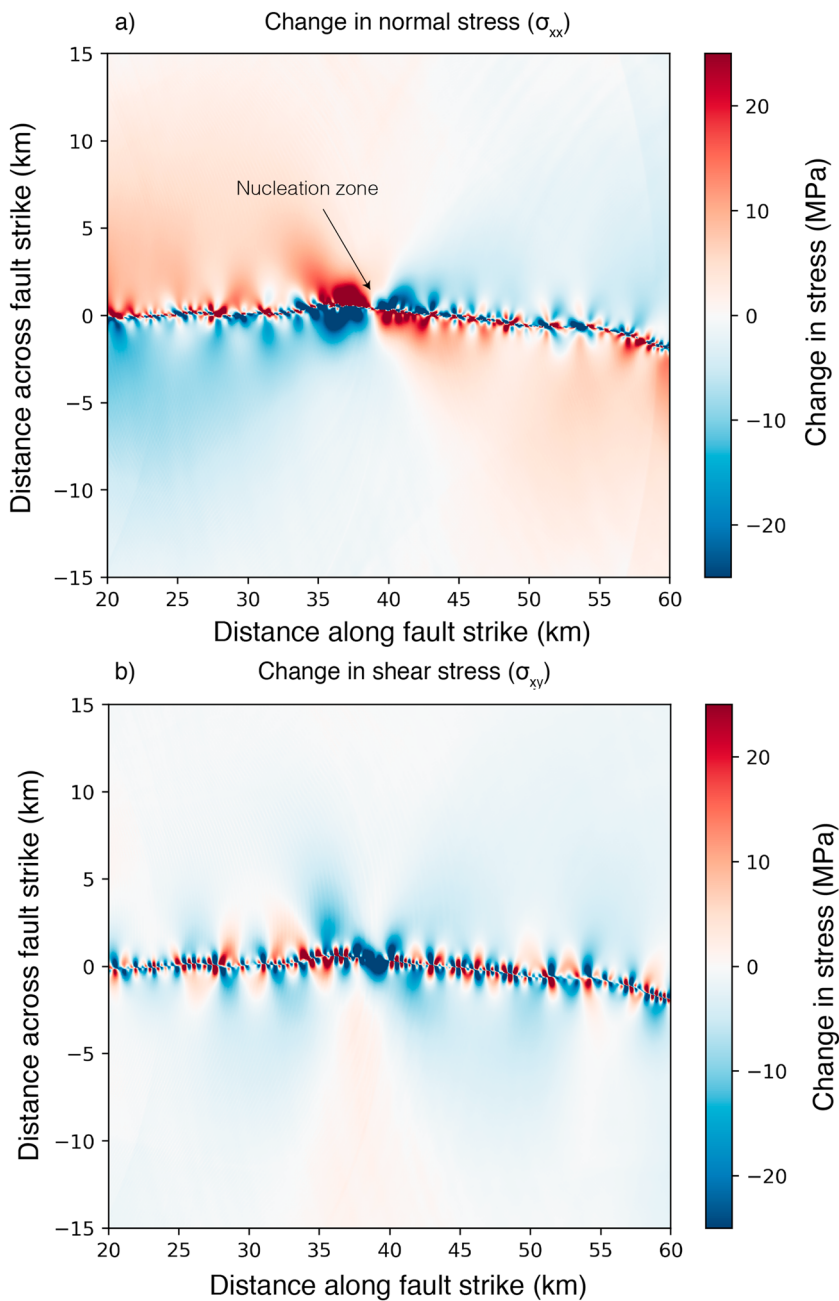


**Figure 4.** Change in stresses at the central part of the domain (taken from 20 to 60 km along fault and -15 to 15 km across fault distance) for a self-affine fault with a Hurst exponent of 0.6 and have normalized root-mean-square deviation from planarity of 0.01. The final shear stress is taken once the simulation reaches a time long enough that there are no dynamic stresses related to the wave propagation and stress change is solely due to static stress changes. This complicated shear stress change will also give a complex Coulomb stress change. (a) Change in normal stresses. The location of the nucleation zone is marked at a distance of 44 km along the fault strike. (b) Change in shear stress for the same realization of the fault profile.

RMS height of 0.01, 93% of the ruptures reaches this distance. Figure 6 shows the PDF of CFF as a function of distance from the fault for different RMS ratios and Hurst exponents. The CFF values are highly variable in the near-fault region and include both positive and negative values. As the distance from the fault increases, the range of CFF values squeeze into a narrow range, and for distances further from the fault, we see CFF values cluster tightly around the mean CFF value. We refer to the approximate distance where we see this transition from a large spread of CFF values to a narrow range as the *threshold distance*. This distance roughly marks the

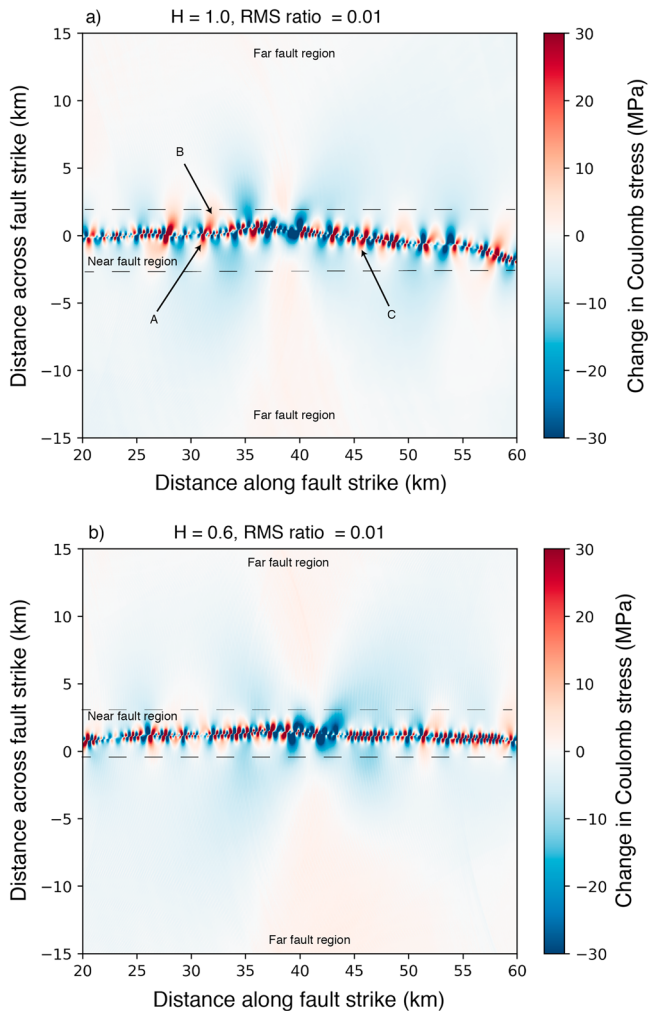


**Figure 5.** Change in Coulomb failure function (CFF) in the central part of domain. (a) The CFF is calculated from the shear and normal stress change (Figure 4) around the fault due to dynamic earthquake slip on the fault. The Hurst exponent of the fault surface is 1.0, and the normalized root-mean-square deviation from planarity is 0.01. The calculations assume an elastic off-fault material with a friction coefficient of  $\mu = 0.4$  and a fault orientation parallel to the overall trace of the main fault. Fault roughness introduces heterogeneous stresses within the main shock rupture area that could promote aftershock production. Positive values indicate increased likelihood of failure, while decreased values are expected to be regions with reduced seismicity. The near-fault and far-fault zones are roughly marked based on the extent of CFF heterogeneity observed in the figure. (b) The CFF is calculated similar to (a) but for a fault surface having a Hurst exponent equal to 0.6 and a normalized rot-mean-square deviation of 0.01.

boundary between the near-fault and intermediate region described above. As is evident from Figure 6, the location of the threshold distance is controlled by the RMS height of the fault profile and it does not depend strongly on  $H$ . Figure 6c shows the results for a smoother fault with an RMS roughness of 0.001, which exhibit an extra band of CFF values that differs from the main band of CFF values. This additional band is due to the hypocentral CFF zones for faults having RMS of 0.001 and reaches distances as large as 5 km away from the fault. The hypocentral zones does not affect the CFF statistics of the positive CFF zones. This is evident in Figure 6, where no extra bands of CFF values are observed towards the positive side of CFF values.

We also analyze the behavior of the mean CFF with distance under different receiver fault orientations. We change the receiver fault orientation successively from  $0^\circ$  to  $20^\circ$  from the main fault and observe the pattern of CFF change with distance for each receiver fault orientation. The behavior of the CFF function with distance does not vary significantly when receiver fault orientation angle is changed, although there is an overall change in the average CFF value at each particular distance.

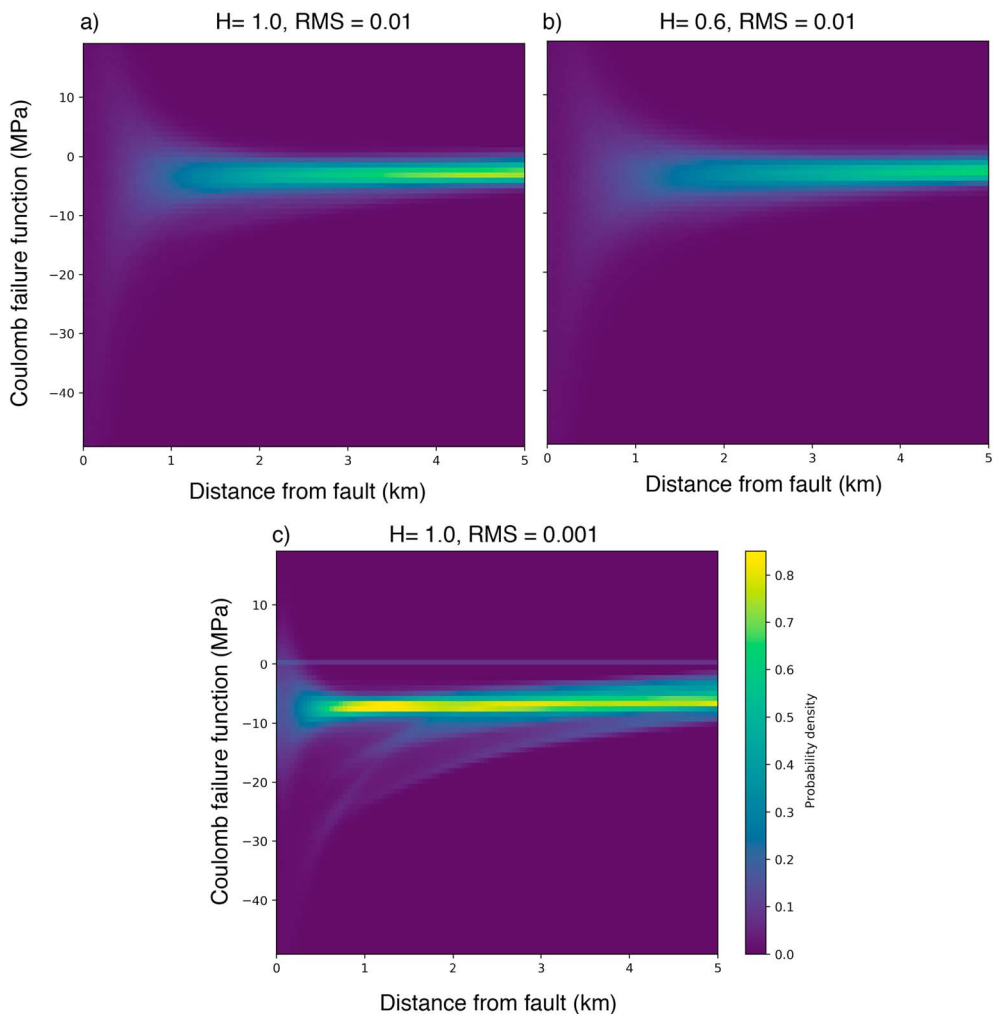


**Figure 6.** The probability density function values of the Coulomb failure function (CFF) relative to the initial stress tensor versus distance away from the fault self-affine fault with a Hurst exponent of 0.6 and a normalized root-mean-square (RMS) deviation from planarity of 0.01. A wider spread of CFF values can be seen near the fault, and this spread squeezes into a narrow band as the distance from the fault increases. This behavior occurs because in the near-fault region, the heterogeneous stress changes due to fault roughness are dominant causing stresses to be highly heterogeneous, while the far-field values collapse to the average stress drop for an earthquake in our suite of simulated events. (a) Probability density function of CFF change for  $H = 1.0$  and RMS of 0.01, (b) same as (a) but for  $H = 0.6$  and RMS of 0.01, and (c) same as (a) but for  $H = 0.6$  and RMS of 0.001. We see an extra band of CFF values that differs from the main band of CFF values. This additional band is due to the hypocentral CFF zones for smoother faults, as the hypocentral zones reach distances as large as 5 km away from the fault. RMS = root-mean-square.

Figure 6 shows one point statistics of our simulation results; however, aftershock zones require rupture of a patch of a particular size. Therefore, to relate our results to aftershock occurrence, we must examine the spatial correlations in the resulting CFF distributions. To examine this question, we calculate the locations as well as lengths of probable aftershock zones using the CFF results. In all of our rough fault scenarios, the probability of occurrence of negative CFF values is greater than the probability of occurrence of positive CFF values. This suggests that we have more zones of seismic inactivity compared to zones of probable aftershock occurrence in the near-fault and intermediate regions. To verify this for the near-fault region, we count total number of positive and negative CFF zones having lengths greater than 500 m at 1.5 km away from the fault in each rupture simulation. Figure 7 shows the number of positive and negative CFF zones in each realization of the fault profile for all 100 fault profiles having  $H = 1$  and RMS ratio 0.01 at a distance 1.5 km away from the fault. We can see that the number of negative CFF zones is greater than the number of positive zones in the near-fault region. Though we observe fewer positive CFF zones when compared to negative CFF zones in the near-fault region, their count (average  $\sim 15$ ) is still much higher than the number of zones we would

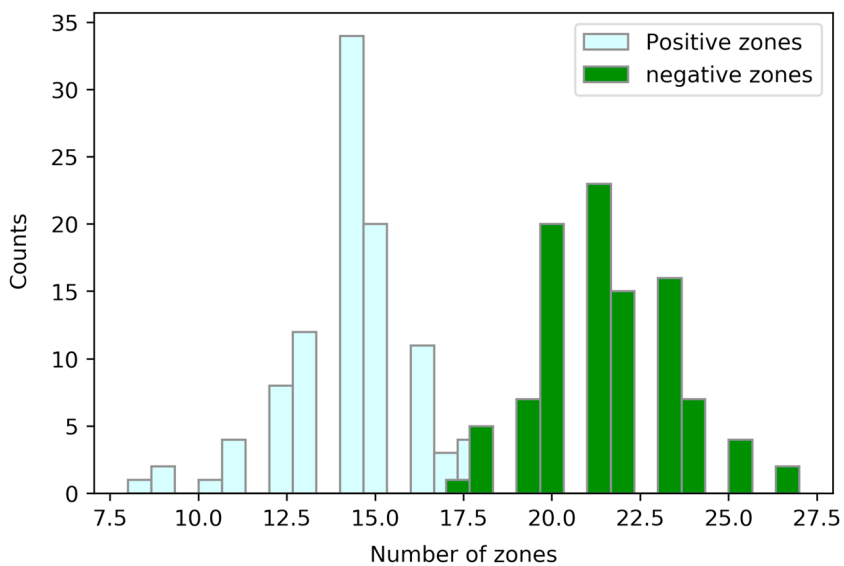


**Figure 7.** The figure shows the histogram constructed of the total number of zones with positive or negative changes in the Coulomb failure function (CFF) in each simulation using data from all the simulations for a rough fault with Hurst exponent equal to 1.0 and a normalized root-mean-square deviation from planarity of 0.01. The data are taken for CFF zones calculated at a distance of 1 km away from the fault in the near-fault region. The positive CFF change zones occur less frequently than the negative CFF change zones, but the number of positive CFF change zones calculated are many times higher than the number that would be calculated using typical static stress calculations. These positive CFF change zones are the zones that static triggering models suggest could host aftershocks of the simulated ruptures.

expect based on typical static stress calculations. These positive CFF zones can potentially trigger earthquakes whose size is small enough to fit in these zones and hence explain aftershocks that appear in stress shadows in static stress calculations based on observational data.

Based on positive CFF zone lengths, we next estimate the maximum magnitude earthquake that each of these zones can host. To do this, we consider the resulting earthquake if each zone were to host a rupture of circular shape and we estimate the rupture area by calculating the length of the rupture at a specific distance away from the fault. Figure 8 shows the possible rupture areas of 5,000 arbitrarily selected positive CFF zones at two different distances away from a fault having  $H = 1$  and RMS ratio of 0.01. The distance away from the fault is chosen so that we can observe the behavior of probable rupture areas both in near-fault region and

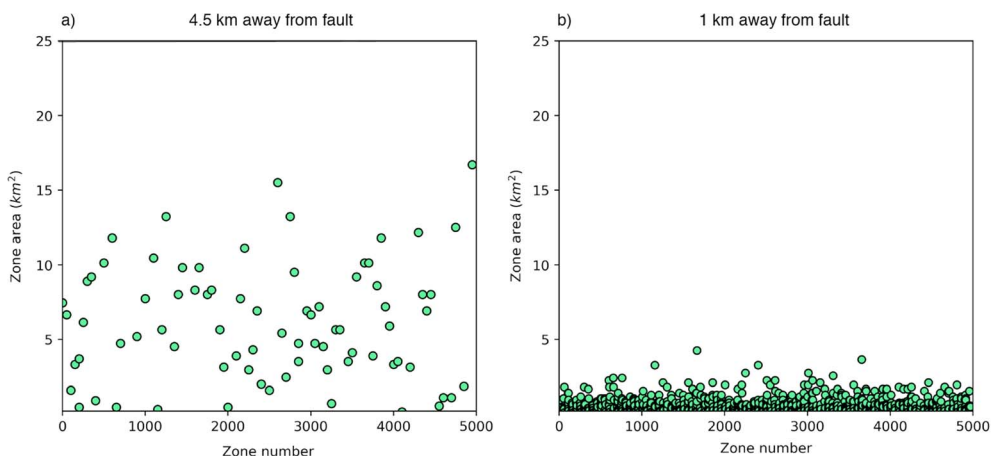


**Figure 8.** Figure shows the modeled maximum rupture areas of positive stress change zone at a particular distance from fault in the near-fault zone. (a) Zone area calculated for positive CFF zones at 4.5 km away from the main fault. (b) Same as (a) but for positive CFF zones at 1 km away from fault. There are more positive CFF zones, that is, the zones prone to aftershocks close to the fault ( $\sim 1$  km), and these zones have smaller areas. Away from the fault ( $\sim 4.5$  km) there are comparatively fewer aftershock prone zones, but these zones tend to be larger than the zones found 1 km from the fault.

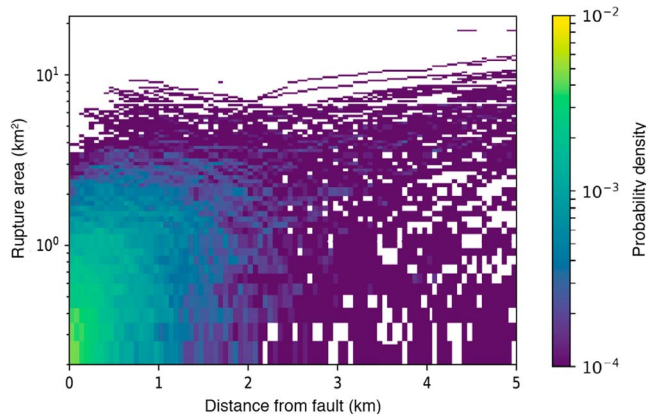


**Figure 9.** The plot shows the spatial distribution of positive stress change zones as a function of distance from the fault. The color scale represents the joint probability density function (PDF) values of both parameters (white color means PDF = 0). Our distance scale in this figure represents the near-fault region and the intermediate region. We find high joint PDF values of smaller probable rupture areas in the near-fault region due to the occurrence of many small positive CFF change zones. There are also some larger probable rupture zones present in this region, though they occur less frequently than the smaller ones. In the intermediate region, both larger and smaller rupture zones have a similar probability of occurrence. For natural earthquakes, an aftershock is not required to fill the entire zone, so we expect that we may still find small earthquakes further from fault.

heterogeneity is likely to be present in the area, which could cause many of these larger CFF zones to host a number of smaller events. This implies that we also expect smaller rupture areas to occur in the intermediate region. We observe from Figure 9 that in the near-fault region for distances  $< 50$  m, there is no positive CFF zone with rupture area larger than  $5 \text{ km}^2$ , suggesting that the probability of occurrence of a larger magnitude aftershock is unlikely at distances extremely close to the main fault. This behavior may also be altered if we relax our assumption of a homogeneous initial stress field. Overall, from Figure 9, we observe that the rupture areas in the near-fault region are mostly below  $10 \text{ km}^2$  with very few reaching above it. In the intermediate region, we see ruptures with comparatively larger rupture areas and some of these rupture areas reach  $19 \text{ km}^2$  in this region.

#### 4. Data Comparison

Our model results describe how the rupture propagation on rough faults perturbs the prevailing stress pattern and defines a spatial CFF pattern in the near-fault region after a major earthquake. We now analyze the observational data of real aftershocks to compare the spatial CFF patterns in our results to those expected for real aftershocks. We take the locations of probable aftershock zones and probable rupture areas from our model results and compare them with the observational aftershock rupture areas and locations. We select five large events from California: the 1984 Morgan Hill Earthquake, the 1989 Loma Prieta Earthquake, the 1992 Landers earthquake, the 1994 Northridge Earthquake, and the 1999 Hector Mine Earthquake. More details about these earthquakes can be found in Table 2. We use relocated earthquake catalogs from Northern and

**Table 2**  
*List of Major Earthquakes Used in This Study*

Earthquake	Mw	Epicenter location	Rupture from
1984 Morgan Hill earthquake	6.2	37.32°N, 121.68°E	Beroza and Spudich (1988)
1989 Loma Prieta earthquake	6.9	37.04°N, 121.88°E	Zeng and Anderson (2000)
1992 Landers earthquake	7.2	34.02°N, 116.43°E	Zeng and Anderson (2000)
1994 Northridge earthquake	6.6	34.21°N, 118.54°E	Zeng and Anderson (2000)
1999 Hector Mine earthquake	7.1	34.59°N, 116.27°E	Salichon et al. (2004)

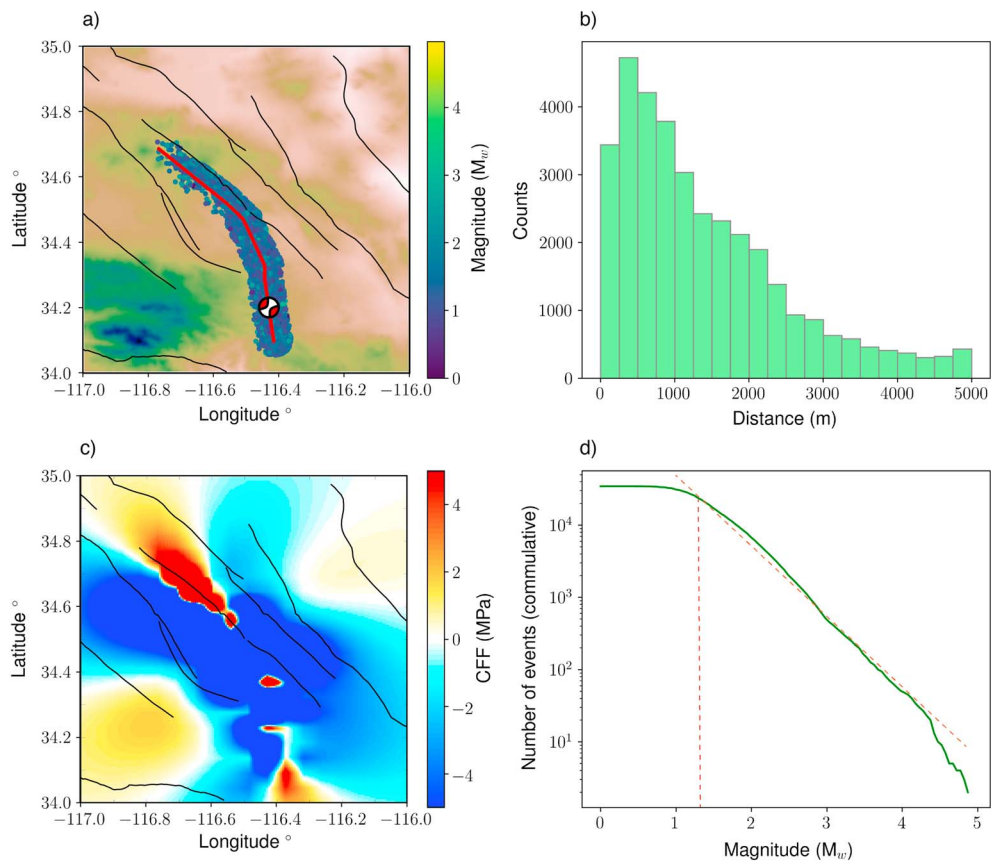


**Figure 10.** Characteristics of the aftershock data for the 1992 Landers Earthquake. (a) Map showing aftershock locations in relation to the surface fault trace of the Landers EQ. The fault trace data are extracted from Zeng and Anderson (2000). The focal mechanism is taken from Global CMT solution (Ekström et al., 2012). Aftershocks occurring within 5 km from the fault trace are also shown with their color representing the magnitude. The black lines in the figure show the locations of active faults in the surroundings of the main ruptured fault. We can see that many faults are approximately parallel to the trace of main fault. (b) The histogram of all aftershock distances from the fault plane. The number of aftershocks decreases as the distance away from the fault increases. (c) The CFF calculated for the 1992 Landers Earthquake at 6 km depth, on the receiver faults, which are parallel to the overall orientation of the main fault. We see few zones of positive CFF change while most part of the near-fault region is dominated by a region exhibiting a stress shadow. (d) The magnitude frequency distribution of the data shown in (a), which follows the Gutenberg-Richter distribution.

Southern California starting in 1984 (Shearer et al., 2005; Waldhauser & Schaff, 2008) to extract the aftershocks associated with these earthquakes. We select a fixed time window 5.5 years after the main earthquake to extract aftershocks. This time window is typically used for a magnitude 7 earthquake in southern California (Allen et al., 1965; Gardner & Knopoff, 1974). Detailed information regarding the rupture of these five events is extracted from slip inversions available through SRCMOD, an online database of finite fault inversions for numerous earthquakes (Mai & Thingbaijam, 2014). We translate the magnitude of aftershocks into rupture areas using an empirical relation derived from Hanks and Bakun (2002). Though there are many alternative relationships to convert magnitude into rupture length (Hanks & Bakun, 2008; Wells & Coppersmith, 1994; Wesnousky, 2008), we select this relationship because it takes into account the scaling of small magnitude earthquakes. We also calculate the rupture areas using the seismic moment and the standard Eshelby formula (Eshelby, 1957) assuming a stress drop of 1 MPa. This choice of stress drop value is typical for faults having geometrical heterogeneities (Bailey & Ben-Zion, 2009) or faults with multistrand fault system geometries (Shaw et al., 2015). The rupture areas calculations using Eshelby (1957) formula are consistent with rupture areas calculations using empirical relation of Hanks and Bakun (2002) and it gives results that are quantitatively similar to those shown here.

We compile a combined data set by considering aftershocks from all five earthquakes described above. We pick only those aftershocks that are located in the region  $<5$  km away from the fault rupture to compare

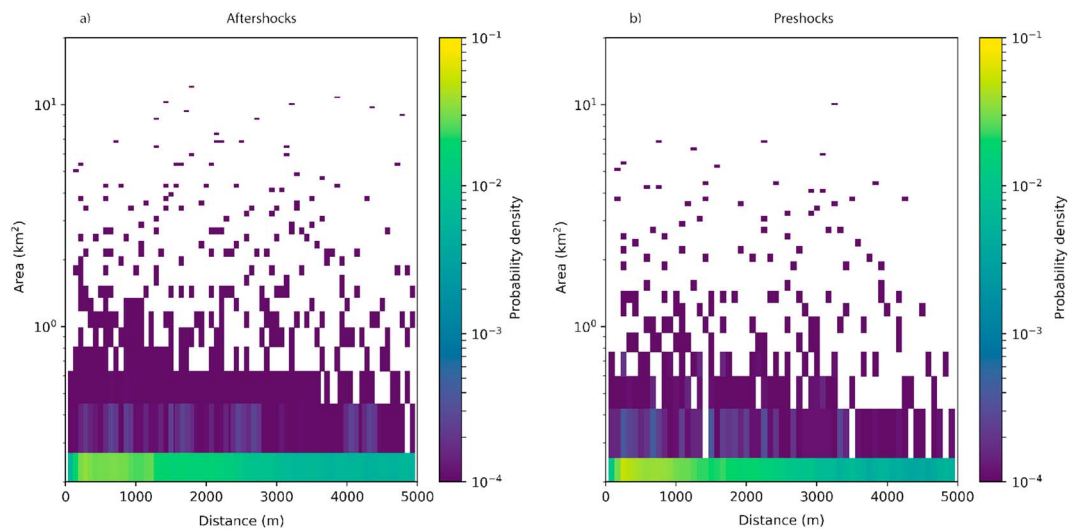


**Figure 11.** Spatial and rupture area distributions for aftershocks and preshocks. (a) Distribution of rupture areas and distance from the main fault plane for all the aftershocks that lie within 5 km of the main rupture in our data set for 5 large earthquakes in California. The data is compiled by combining aftershocks from the 1984 Morgan Hill earthquake, the 1989 Loma Prieta earthquake, the 1992 Landers earthquake, the 1994 Northridge earthquake, and the 1999 Hector mine earthquake. (b) Same as (a), but for events occurring for 5.5 years prior to the same large earthquakes except the 1984 Morgan Hill earthquake. Both data sets in (a) and (b) are similar with no preference for particular magnitudes at certain distance from the fault. This suggests that stresses in the near-fault region are dominated by stress heterogeneity caused by fault roughness over repeated earthquake cycles. The smaller magnitude earthquakes pattern in the near-fault region does not vary much during postseismic or preseismic phase, suggesting that the existing stress field is always very heterogeneous prior to a large earthquake in a manner similar to that found in our simulations.

them with our near-field model results. There are also some additional aftershocks present at distances  $> 5$  km from fault, but we do not consider those since those aftershocks do not provide us any information about the near-fault stress field. Additionally, because the minimum zone length that we consider has an area of approximately  $0.2 \text{ km}^2$ , we only consider events with  $M > 3$ , which corresponds to this minimum area. Figure 10a shows the aftershocks for the 1992 Landers earthquake. Due to the Gutenberg-Richter magnitude-frequency distribution (Gutenberg & Richter, 1944), we see most aftershocks with  $M_w < 2$ . The histogram with respect to distance of these aftershocks (Figure 10b) shows that most of these aftershocks are located very close to the fault. Among all of the events, most of the aftershocks occur between 450 and 500 m away from fault. The magnitude-frequency distribution of the aftershocks shown in Figure 10a is shown in Figure 10d. We note that the magnitudes of the aftershocks follow the GR distribution. We also calculate the CFF using the slip model from Wald and Heaton (1994) for the 1992 Landers earthquake for faults parallel to the main fault. Figure 10c shows the CFF at 6 km depth, that is, the focal depth of the 1992 Landers earthquake. We see a prominent stress shadow in the middle of the fault with few positive CFF zones within the main slip area of the fault.

To understand the behavior of the rupture areas as a function of distance, we plot the joint PDF of the rupture area with distance away from fault from our complete compiled data set. This plot is analogous to Figure 9, but shows observational data rather than our modeling results. As shown in Figure 11a, we see a similar behavior to what is observed in our modeling results. Rupture zones with all rupture areas (i.e., both smaller [ $< 0.45 \text{ km}^2$ ] and larger [ $\geq 0.45 \text{ km}^2$ ]) are present in near-fault as well as intermediate regions. The smaller rupture lengths are more probable in the near-fault region than the larger rupture lengths, similar to our modeling results. In the intermediate region, we see a relatively high probability of smaller rupture lengths when compared to the larger rupture lengths. Since our modeling results do not preclude smaller events in the large positive CFF zones, we believe that our model is consistent with the higher probability of smaller rupture areas in the intermediate region, though this behavior is not reflected in the probability values in Figure 9. Figure 12 shows the histograms with respect to distance of aftershocks for two different minimum magnitudes from our complete compiled data set. Based on the comparison of these histograms, we find that the aftershocks in the near-fault region follow the GR distribution, with an order of magnitude more aftershocks with  $M_w > 2$  than aftershocks with  $M_w > 3$ . As seen in Figure 9, the fault roughness produces many zones of positive stress

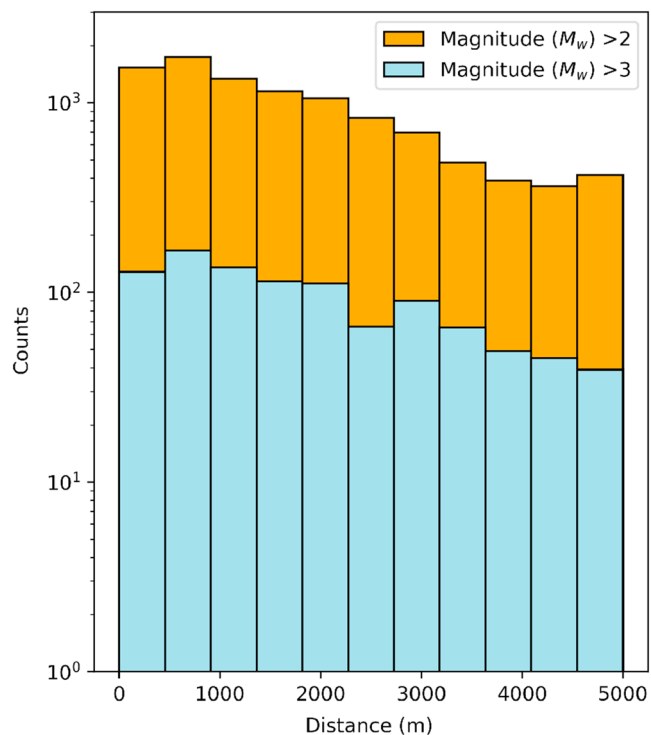


**Figure 12.** A comparison of histograms of aftershock distances from the fault plane for two different magnitude ranges. The histogram of aftershock distances from the fault plane for aftershocks with  $M_w > 3$  is shown in blue while the histogram of aftershock distances from the fault plane for aftershocks with  $M_w > 2$  is shown in orange color. The aftershocks data set for both histograms is compiled by combining the aftershocks from the 1984 Morgan Hill earthquake, the 1989 Loma Prieta earthquake, the 1992 Landers earthquake, the 1994 Northridge earthquake, and the 1999 Hector mine earthquake. The aftershocks follow the GR distribution at all distances from the fault with an order of magnitude more aftershocks with  $M_w > 2$  than aftershocks with  $M_w > 3$ . Our model suggests this arises due to the fault roughness producing zones of positive stress change of a variety of lengths at all distances from fault, and that these zones can host many smaller events to produce the GR distribution of event sizes.

change with a variety of lengths, and these zones can host many smaller events which will thus produce the GR distribution of event sizes.

To compare our results to seismicity that did not occur in response to an earthquake, we compile a combined data set by considering events that occurred on the same faults hosting the large earthquakes, with the exception of the 1984 Morgan Hill earthquake due to the start time of the catalog. We select the same time window (5.5 years) for these events. We plot the joint PDF as seen in Figure 11b of the rupture areas (calculated from  $M_w$  of preshocks) with distance from fault and see similar behavior to what is observed for aftershocks. For preshock data, we again see ruptures with all lengths in both the near-fault and intermediate regions. Similar to the aftershock data, the smaller rupture lengths are seen to be more probable in the near-fault as well as the intermediate regions when compared to the larger rupture lengths. This suggests that the earthquake stress change did not influence the general decay with distance of earthquakes in the mainshock rupture area, only the temporal characteristics. This suggests that a heterogeneous stress field likely exists throughout the seismic cycle, and its spatial characteristics are not strongly changed by a single earthquake. Rather, a heterogeneous stress field is maintained and reinforced by complex slip patterns on successive large earthquakes on rough faults.

## 5. Discussion and Conclusions

In this work we investigate the occurrence of aftershocks which cannot be explained by traditional static stress change calculations (Beroza & Zoback, 1993; Kilb et al., 1997) or which nucleate in the zones of stress shadows (Segou & Parsons, 2014). We perform dynamic rupture simulations on many realizations of rough faults where the roughness parameters are taken from observational studies (Candela et al., 2012). For each realization of the fault profile, we obtain the static stress change in the volume and then estimate the spatial distribution of

static stress change due to dynamic fault slip surrounding the main fault. We observe that the pattern of static stress change is highly complex (Chester & Chester, 2000; Dieterich & Smith, 2009) in the near-fault regions with negative values of stresses more prevalent than positive values. The width of the region where stresses are highly complex depends on the RMS ratio of the fault roughness. We do not find a strong dependence of the width of near-fault region on the  $H$  value.

The zones of negative CFF (i.e., the zones not susceptible to aftershocks) are more prevalent in the far-fault and intermediate regions but many of those zones also exist in the near-fault region. In addition to negative CFF zones, there are many positive CFF zones present in the near-fault region. These zones are of particular importance since these are the zones which are locations of potential aftershocks. We count the number of positive CFF zones having length  $> 500$  m in the near-fault region at different distances away from the fault. Based on our data, the average number of total positive CFF zones found in a single earthquake simulation is  $\sim 15$  in the middle of near-fault region. This value is many times higher than the positive CFF zones found from the usual static stress calculations (e.g., (Lin & Stein, 2004; Toda et al., 1998; Toda et al., 2008)) in the near-fault region. Since the positive CFF zones have the capability to host earthquakes whose size is small enough to fit in these zones, they could host earthquakes that appear in zones of stress shadows in static stress calculations in the near-fault region. However, similar seismicity pattern are observed prior to the mainshocks, suggesting that general stress heterogeneity also exists throughout the seismic cycle and plays an important role in earthquake occurrence.

Furthermore, we calculate the rupture area of each positive CFF zone by considering the possibility that each zone were to host a rupture of circular shape and observe that smaller rupture areas are more dominant inside the near-fault region than the large rupture areas. This is because we have a larger fraction of small positive CFF zones close to the fault due to the fault roughness effects prevailing in this region. The equivalent areas in the near-fault region are mostly below  $10 \text{ km}^2$ . In the intermediate region, where the fault roughness effects are less important, we see fewer positive CFF zones but larger areas when compared to the near-fault region. Based on our modeling results, we conclude that the aftershocks occurring in the near fault region of a rough fault are result of complex static stress change pattern resulting from the stress heterogeneities introduced by fault roughness over many seismic cycles.

Our comparison between aftershock data and preshock data provides a method for understanding how the stress perturbations due to fault roughness affect the seismicity patterns in the near-fault region. We see that both aftershocks and preshocks show similar spatial characteristics, suggesting the stress heterogeneities driving their occurrence are similar. Based on the similarities of behavior of both data sets, we believe that stresses in the near-fault region are always heterogeneous as suggested by some other observational studies using InSAR and GPS data (Erlingsson & Einarsson, 1989; Pedersen et al., 2003). Our results show that these near-fault stresses are dominated by stress perturbations caused by fault roughness throughout the history of the earthquake cycle. We suggest that the locations of small ruptures (either as preshocks or aftershocks) are independent of their timing relative to an earthquake in the near-fault region and are predominately controlled by the stress heterogeneities imposed by fault surface complexity. The occurrence of small aftershocks at all distances from the main fault in the observational data suggests that heterogeneous stress can cause multiple small events within a patch of increased CFF due to earthquake slip. The pattern of smaller magnitude earthquakes in the near-fault region does not change between the postseismic and preseismic phases, suggesting that the existing stress field is always very heterogeneous.

Aftershock distribution and static stress changes in the context of rough faults has been modeled by many previous studies. Bailey and Ben-Zion (2009) used a quasi-static modeling approach to model the stress drop due to an earthquake on a geometrically heterogeneous fault. They showed that spatial heterogeneity of the fault surface causes the stress drop to significantly reduced (an order of magnitude lower) as compared to traditional estimates with a homogeneous fault. Smith and Dieterich (2010) performed quasi-static modeling with heterogeneous fault geometry to capture the occurrence of aftershocks in stress shadows and temporal changes in the focal mechanisms of aftershocks. Shaw et al. (2015) used a quasi-static modeling approach with a multistrand fault system geometry to explain the reduced ground motions for aftershocks observed in the near-fault regions. They showed that the observed reduced ground motions in the near-fault region are due to the smaller stress drop of aftershocks (compared to mainshock of similar magnitude events) in this region. Our results agree with these static calculations in terms of the general statistical trends that emerge when stress changes are averaged along strike and over many ruptures. Further work is needed to assess the

similarities of the predictions for individual events, and if the stress changes exhibit the same variability along strike when dynamic rupture effects are included.

The near-fault zone of natural faults exhibits a complex damage pattern (Andrews, 2004, 2005; Faulkner et al., 2003; Myers & Aydin, 2004; Rice et al., 2005), and this pattern may further introduce second order stress perturbations. The near-fault region of high damage (sometimes referred to as a weak zone) is observed to strongly influence the geographical distribution of seismicity both before and after a major earthquake (Hauksson, 2011, 2010). Powers and Jordan (2010) showed that the width of this near-fault region of high damage is controlled by the stress variations caused by the fault roughness. Our results also show that the width of the near-fault region and stress field heterogeneity (which in turns control the geographical distribution of seismicity) is controlled by the roughness of the fault and that this roughness computed dynamically gives similar results to quasi-static calculations. Some discrepancies in our model results and real data may arise due to the secondary static stress changes (secondary triggering) associated with the secondary earthquakes (aftershocks) that occur as a result of a major earthquake (Meier et al., 2014). Some studies suggest that every single earthquake has its role in redistributing the prevailing static stresses (Kagan, 1994; Meier et al., 2014; Marsan, 2005; Hanks, 1992; Helmstetter et al., 2005), an effect not captured by our simulations. A further effect influencing the off-fault stresses include yielding of the off-fault material due to plastic deformation (Andrews, 2005; Dunham et al., 2011a, 2011b; Gabriel et al., 2013; Shi & Day, 2013) that may alter the spatial pattern of stress change. This topic will be the subject of future work.

We assumed a predefined single receiver fault orientation to calculate static stress changes. Since the realistic fault systems do not always include parallel faults, calculating the static stress change with multiple receiver fault orientations may improve the spatial distributions of aftershocks. Hainzl et al. (2010) showed that their aftershock model with multiple receiver fault orientations showed a good agreement with directly triggered aftershocks from 1992  $M7.2$  Landers earthquake. We will consider calculating the CFF using multiple receiver faults in future work, using calculated fault orientations from the off-fault damage. This method will address the open question regarding if the spatial decay of seismicity is due to the stress field or the damage zone. This approach can also examine if the fault orientations derived from dynamic simulations provide additional benefits over those assumed in static calculations.

The stress changes due to coseismic slip on an earthquake can cause a pore-pressure variation in the region surrounding the main fault which can change the strength of host faults to initiate further earthquakes (Chen et al., 2012; El Hariri et al., 2010; Gupta, 2002; Nur & Booker, 1972). Furthermore, the diffusion of pore-pressure can cause seismicity to migrate over time (Chen et al., 2012; El Hariri et al., 2010). Similarly, a time-dependent increase in pore pressure due to passing seismic waves can also increase seismicity of a region as observed in many locations with geothermal or volcanic activity (Hill et al., 1993; Freed, 2005). Aseismic slip can also modify the stresses on the fault and bring it close to failure, changing seismicity over time (Vidale et al., 2006; Vidale & Shearer, 2006) and causing more aftershocks to occur. Constraining the effect of fluid flow and aseismic slip on the aftershock triggering is a challenging problem (El Hariri et al., 2010; Vidale et al., 2006; Vidale & Shearer, 2006), and in particular isolating the role of each of these mechanisms in aftershock triggering is not straightforward (Lohman & McGuire, 2007; Vidale & Shearer, 2006). Some studies suggest that both of these mechanisms work together (Hainzl, 2004; Waite & Smith, 2002) and are common in areas of earthquake bursts and swarms (Vidale et al., 2006; Vidale & Shearer, 2006; Hainzl, 2004). We do not model the pore pressure or aseismic slip, and our observational data may include effects from these mechanisms. Additionally, the observational data may include effects from heat flow, topography,  $V_p/V_s$  ratio, crustal thickness (Hauksson, 2011), and material contrasts (Rubin & Ampuero, 2007; Rubin & Gillard, 2000) which we did not consider in this study. However, we note that our results are consistent with overall trends in the spatial locations of seismicity, suggesting these additional mechanisms may be more important for describing the transient behavior of aftershocks rather than their spatial occurrence patterns.

Our simulations are in 2-D but real earthquakes occur on faults in 3-D, an effect which is not captured in the present study. By running simulations in 3-D, the rupture process will not always be coherent in the third direction (Dunham et al., 2011a; Shi & Day, 2013), which may cause some differences in the stress change pattern surrounding a fault compared to our 2-D model results. Our initial simulations are in 2-D due to the fact that 3-D simulations are much more computationally expensive. We have also assumed that the initial stress state is uniform in space, which neglects the previous deformation history of the fault, including the interseismic phase of the seismic cycle to build up stresses to the level of failure. Our results suggest this background

heterogeneity is important, and it is possible that we can quantitatively account for this history of stress heterogeneity by deriving the initial stress state from a long term tectonic model to initiate our model with stresses that are consistent with the slip history of the fault at the start of our simulation. This is a much more challenging computational problem, since the model must resolve both the slow loading of the interseismic period and the rapid slip during the coseismic period, and will be addressed in subsequent work.

Focal mechanisms provide a method to examine the stress orientations compatible with the radiation pattern of a particular earthquake (e.g., (Hardebeck et al., 1998; Hardebeck, 2010, 2015; Meier et al., 2014; Steacy et al., 2004), but since in most cases the focal plane is ambiguous (Nandan et al., 2016), there is always uncertainty involved in determining fault plane orientations and hence the resulting static stresses. Moreover, the alignments of focal mechanisms may not always follow a particular pattern. For instance, large variability of primary focal mechanisms of aftershocks was observed by Mallman and Parsons (2008) during an investigation of worldwide  $M > 7$  earthquakes. Similarly, focal mechanisms following the 1989 Loma Prieta earthquake are diverse and are not aligned with the directions expected for static stress triggering (Beroza & Zoback, 1993; Kilb et al., 1997). While the heterogeneity of alignments of focal mechanisms introduces uncertainty in determining static stresses, this heterogeneity has been proven useful in many cases, for example, the case of central and southern California region, where this heterogeneity has been used to learn the long-term evolution of fault zones and their seismic behavior (Bailey et al., 2010). Similarly, this heterogeneity has been used to estimate the crustal stress heterogeneity in southern California (Smith & Heaton, 2011). Additionally, the effects of static stress changes are not always straightforward to reconcile with subsequent seismicity, such as a spatial correlation observed between stress shadows and seismicity rate reduction (Toda et al., 2012) at one point in space while a complete absence of a stress shadow (Felzer & Brodsky, 2006) may occur in another region.

Based on our results of dynamic rupture modeling, we relate the spatial distribution of aftershocks in the near fault region of a rough fault to its fractal geometry. Our results provide improved constraints on the magnitude and spatial distributions of aftershock occurrence, which help scientists better understand the basic physics of earthquake interaction and spatial locations of earthquakes in general, an important concern of current earthquake science (Cocco & Rice, 2002; King et al., 2001; Hill et al., 2002). Such knowledge is essential for improving estimates of future hazard and risk in earthquake-prone areas worldwide.

## Appendix A: Self-Similar and Self-Affine Profiles

Self-similar profiles are curves that show identical characteristics regardless of the scale of view (i.e., zooming in or out is equivalent to rescaling the length and height by the same factor), while self-affine fractals require rescaling the length and height by different factors to obtain similar statistical profiles (Russ, 1994). Self-similar is thus a specific case of self-affine where the RMS height fluctuation of the profile is proportional to the length of the profile. Earlier studies (Brown & Scholz, 1985; Lee & Bruhn, 1996; Power & Tullis, 1995) suggest that natural fault surfaces are self-similar fractals. More recent studies (Brodsky et al., 2011; Candela et al., 2012; Candela et al., 2009; Candela et al., 2011; Sagy et al., 2007; Renard et al., 2006) are able to provide very high resolution fault roughness measurements. Some of these measurements suggest that fault surfaces in both the slip-parallel and slip-perpendicular direction are self-affine fractals, though other authors suggest that self-similar profiles provide a better overall description of the fault geometry (Shi & Day, 2013).

We use two parameters to describe fault roughness. The first parameter is the Hurst exponent, denoted by  $H$ , which quantifies the self-affine scaling of the fault profile. For a self-affine fractal, if we rescale the horizontal scale by a factor  $x$ , then the vertical scale is rescaled by factor  $x^H$  (for the self-similarity case  $H = 1$ ). The second parameter specifies the actual height of fault curve relative to a planar fault. One such parameter that quantifies the amplitude is the RMS deviation of a fault profile from planarity. The RMS height ( $h_{rms}$ ) for a 1-D self-affine fault profile ( $y = f(x)$ ) with length  $L$  can be defined as

$$h_{rms} = \sqrt{\frac{1}{L} \int_{-L/2}^{L/2} f^2(x) dx}. \quad (A1)$$

Equation A1 considers all the wavelengths of roughness that are smaller than  $L$ . The RMS height is related to the maturity of the fault as the roughness amplitude of the fault varies when the fault progresses from immature to mature. The value of  $H$  varies from 0.6 to 1 for observed fault surfaces while the RMS height to

wavelength ratio has values between  $10^{-2}$  to  $10^{-3}$  depending upon the maturity of the fault (Brodsky et al., 2011). A smaller value of  $H$  indicates that the faults appears rougher when viewed at decreasing scales and a smaller value of RMS height indicates a smoother fault profile. It is also important to note that the RMS height is the same at all scales for self-similar fractals, but it is scale dependent for self-affine fractals (Aviles et al., 1987; Brown & Scholz, 1985; Okubo & Aki, 1987; Power et al., 1988). In this study, we use the RMS height at the largest scale to quantify roughness for self-affine profiles. The Hurst exponent is related to power spectral density for self-affine fractals:

$$p(k) \propto k^{-1-2H}. \quad (\text{A2})$$

Here  $p(k)$  is the spectral density,  $k$  is the wave number given by  $k = \frac{2\pi}{\lambda}$ . In the case of a self-similar profile,

$$p(k) = ck^{-3}. \quad (\text{A3})$$

Here  $c$  is given by  $2\pi^3\gamma^2$ . The parameter  $\gamma$  is the RMS height to wavelength ratio. Figure S1 in the supporting information shows spectral density plot for one dimensional (1-D), self-similar fault and self-affine fault profiles.

## Appendix B: Rupture Nucleation Procedures

We nucleate ruptures in the areas where the ratio of shear to normal stress is highest after filtering out the high frequency variations associated with the small scale roughness (Fang & Dunham, 2013). We expect such locations to be representative of the regions on natural faults where ruptures are likely to initiate. In all of our simulations, we start rupture near the center of the fault. We do this by generating many fault profiles and then calculating the ratio of shear to normal stress at each point on the fault. If the ratio is highest between 35 to 45 km along fault distance, then we consider the fault profile for further rupture simulation, otherwise we discard the profile and generate a new one.

The SW friction law has been used with a variety of different nucleation strategies to initiate ruptures (Andrews, 1985; Bizzarri & Cocco, 2005; Day, 1982; Dunham & Archuleta, 2005; Ionescu & Campillo, 1999). These different nucleation strategies could potentially affect the rupture propagation process and therefore the final stress field. Studies such as Bizzarri (2010) have quantified this effect by comparing the process of rupture propagation and resultant surface ground motions for ruptures with different nucleation strategies. We vary our rupture nucleation strategy for a single realization of each fault profile to ensure that our results do not depend on the nucleation method. We use three different techniques to initiate rupture, (1) time-independent overstressing of the fault a method used in early SCEC rupture code problems (Harris et al., 2009), (2) time-dependent overstressing of the fault, and (3) overstressing a single grid point within a critically stressed nucleation patch a method similar to (Schmedes et al., 2010). In the first technique, we select a 3-km fault patch and raise the shear traction on each point of the fault patch to  $1.01T_f^{(i)}$ . Here  $T_f^{(i)}$  is the failure traction on  $i$ th point on the fault, and is given by  $\mu_s T_n^{(i)}$ , where  $T_n^{(i)}$  is the normal traction on  $i$ th point on the fault. In the second technique, we again select a 3 km fault patch and linearly raise the shear traction with time on each point within it to  $1.01T_f^{(i)}$  over an onset time of 0.87 s. In the last technique, we select a 3-km fault patch and raise the shear traction on each point of this patch just below the failure traction ( $0.999T_f^{(i)}$ ) while the shear traction on the central grid point of the fault patch is raised to a traction value of  $1.01T_f^{(i)}$ .

Once we run simulations with each of these nucleation strategies, we compare the ground motions resulting from these strategies at six synthetic station locations on each side of the fault. Three of these station locations reside in the near-fault region while three reside in far-fault region. In our modeling setup, the region having distance  $< 3$  km from fault can be considered as the near-fault region while region having distance  $> 5$  km as the far-fault region. Our reason for considering these regions separately is due to the differences we find in the static stress changes, as discussed in the results section. We compare two properties of the seismic signal: the amplitude of the first arriving compressional ( $P$ ) wave, and the peak ground velocity (PGV) of the signal at those stations. In addition, we also compare the final slip distribution from ruptures initiated using the nucleation strategies mentioned above. Based on our comparison at the selected grid resolution ( $\Delta x = 25$  m), we find the amplitude of the  $P$  wave as well as the PGV value to be in a similar range for all of our nucleation strategies at each station. The average difference between the amplitude of the  $P$  wave and the PGV is

less than 10%; for both near-fault and far-fault regions. We also do not find any significant difference in the slip history to prefer any particular strategy. Therefore, we default to the simplest strategy of a statically overstressed nucleation patch for our full set of simulations.

## Appendix C: CFF Calculation

The CFF (King et al., 1994) can be calculated using the following equation

$$\Delta CFF = \Delta\tau_\beta - \mu_\beta \Delta\sigma_\beta. \quad (C1)$$

Here  $\Delta CFF$  is the change in CFF on a receiver fault due to static stress changes introduced by the earthquake on the main fault,  $\Delta\tau_\beta$  is the shear stress change introduced on the same receiver fault plane,  $\mu_\beta$  is the effective friction coefficient of the receiver fault (a combination of the friction coefficient and Skempton's coefficient (Skempton, 1954) describing poroelastic effects), and  $\Delta\sigma_\beta$  is the change introduced in normal stress on the receiver fault plane. It is important to note that  $\tau_\beta$  and  $\sigma_\beta$  are determined by resolving the stress tensor onto the desired receiver fault plane surrounding the main fault.

We choose the orientation of all the receiver faults to be parallel to the overall trace of the main fault. This assumption will not necessarily be true for every case, but we believe that it is reasonable to assume that aftershocks occur on structures formed due to the same tectonic history as the main fault. Additionally, field studies also reveal parallel faults in strike-slip fault zones such as those observed for the Carboneras Fault Zone in Spain (Faulkner et al., 2003). All of our calculations assume  $\mu_\beta = 0.4$ , a value close to the average of the friction values (average of  $\mu_s$  and  $\mu_d$ ) on the main fault. This value is typically used in the literature for strike-slip or unknown faults (Parsons et al., 1999), and receiver fault orientations parallel to the trace of the main fault. If the calculated values of CFF are positive, it indicates increased likelihood of failure, while decreased values are expected to indicate stress shadows or regions with reduced seismic activity. We combine the calculated CFF values from all realizations of each set of fractal characteristics to compute point statistics.

## Acknowledgments

This research was supported by the Southern California Earthquake Center (Contribution 8864). SCEC is funded by NSF Cooperative Agreement EAR-1033462 & USGS Cooperative Agreement G12AC20038. We are grateful to the University of Memphis High Performance Computing Center for providing computing facilities to run our simulations. The Northern California Earthquake Catalog and Southern California Earthquake Catalog are freely available online through [http://www.ledo.columbia.edu/\\$sim\\$felixw/NCAeqDD/](http://www.ledo.columbia.edu/$sim$felixw/NCAeqDD/) and <http://scedc.caltech.edu/research-tools/alt-2011-dd-hauksson-yang-shearer.html>. The rupture code is available on GitHub (<https://github.com/egdaub/fdfault>). We also thank two anonymous reviewers and associate editor Yoshihiro Kaneko for comments that helped improve this manuscript.

## References

- Aki, K. (1972). Earthquake mechanism. *Tectonophysics*, 13(1–4), 423–446.
- Allen, C. R., Amand, P. S. t., Richter, C., & Nordquist, J. (1965). Relationship between seismicity and geologic structure in the Southern California region. *Bulletin of the Seismological Society of America*, 55(4), 753–797.
- Allmann, B. P., & Shearer, P. M. (2009). Global variations of stress drop for moderate to large earthquakes. *Journal of Geophysical Research*, 114, B01310. <https://doi.org/10.1029/2008JB005821>
- Andrews, D. (1976). Rupture propagation with finite stress in antiplane strain. *Journal of Geophysical Research*, 81(20), 3575–3582.
- Andrews, D. (1985). Dynamic plane-strain shear rupture with a slip-weakening friction law calculated by a boundary integral method. *Bulletin of the Seismological Society of America*, 75(1), 1–21.
- Andrews, D. (2004). Rupture models with dynamically determined breakdown displacement. *Bulletin of the Seismological Society of America*, 94(3), 769–775.
- Andrews, D. (2005). Rupture dynamics with energy loss outside the slip zone. *Journal of Geophysical Research*, 110, B01307. <https://doi.org/10.1029/2004JB003191>
- Andrews, D., & Barall, M. (2011). Specifying initial stress for dynamic heterogeneous earthquake source models. *Bulletin of the Seismological Society of America*, 101(5), 2408–2417.
- Aochi, H., Fukuyama, E., & Matsu'ura, M. (2000). Selectivity of spontaneous rupture propagation on a branched fault. *Geophysical Research Letters*, 27(22), 3635–3638.
- Aviles, C., Scholz, C., & Boatwright, J. (1987). Fractal analysis applied to characteristic segments of the San Andreas fault. *Journal of Geophysical Research*, 92(B1), 331–344.
- Bailey, I., & Ben-Zion, Y. (2009). Statistics of earthquake stress drops on a heterogeneous fault in an elastic half-space. *Bulletin of the Seismological Society of America*, 99(3), 1786–1800.
- Bailey, I. W., Ben-Zion, Y., Becker, T. W., & Holschneider, M. (2010). Quantifying focal mechanism heterogeneity for fault zones in central and southern California. *Geophysical Journal International*, 183(1), 433–450.
- Beeler, N., Tullis, T., & Goldsby, D. (2008). Constitutive relationships and physical basis of fault strength due to flash heating. *Journal of Geophysical Research*, 113, B01401. <https://doi.org/10.1029/2007JB004988>
- Ben-Zion, Y., & Lyakhovsky, V. (2006). Analysis of aftershocks in a lithospheric model with seismogenic zone governed by damage rheology. *Geophysical Journal International*, 165(1), 197–210.
- Beroza, G. C., & Spudich, P. (1988). Linearized inversion for fault rupture behavior: application to the 1984 Morgan Hill, California, earthquake. *Journal of Geophysical Research*, 93(B6), 6275–6296.
- Beroza, G. C., & Zoback, M. D. (1993). Mechanism diversity of the Loma Prieta aftershocks and the mechanics of mainshock-aftershock interaction. *Science*, 259(5092), 210–213.
- Bizzarri, A. (2010). How to promote earthquake ruptures: Different nucleation strategies in a dynamic model with slip-weakening friction. *Bulletin of the Seismological Society of America*, 100(3), 923–940.

- Bizzarri, A., & Cocco, M. (2005). 3D dynamic simulations of spontaneous rupture propagation governed by different constitutive laws with rake rotation allowed. *Annals of Geophysics*, 48(2), 279–299.
- Brodsky, E. E., Gilchrist, J. J., Sagy, A., & Collettini, C. (2011). Faults smooth gradually as a function of slip. *Earth and Planetary Science Letters*, 302(1), 185–193.
- Brown, S. R., & Scholz, C. H. (1985). Broad bandwidth study of the topography of natural rock surfaces. *Journal of Geophysical Research*, 90(B14), 12,575–12,582.
- Bruhat, L., Fang, Z., & Dunham, E. M. (2016). Rupture complexity and the supershear transition on rough faults. *Journal of Geophysical Research: Solid Earth*, 121, 210–224. <https://doi.org/10.1002/2015JB012512>
- Candela, T., Renard, F., Bouchon, M., Brouste, A., Marsan, D., Schmittbuhl, J., & Voisin, C. (2009). Characterization of fault roughness at various scales: Implications of three-dimensional high resolution topography measurements. In Y. Ben-Zion & C. Sammis (Eds.), *Mechanics, Structure and Evolution of Fault Zones* (Vol. 116, pp. 1817–1851). Birkhäuser Basel: Springer.
- Candela, T., Renard, F., Bouchon, M., Schmittbuhl, J., & Brodsky, E. E. (2011). Stress drop during earthquakes: Effect of fault roughness scaling. *Bulletin of the Seismological Society of America*, 101(5), 2369–2387.
- Candela, T., Renard, F., Klinger, Y., Mair, K., Schmittbuhl, J., & Brodsky, E. E. (2012). Roughness of fault surfaces over nine decades of length scales. *Journal of Geophysical Research*, 117, B08409. <https://doi.org/10.1029/2011JB009041>
- Chen, X., Shearer, P., & Abercrombie, R. (2012). Spatial migration of earthquakes within seismic clusters in southern California: Evidence for fluid diffusion. *Journal of Geophysical Research*, 117, B04301. <https://doi.org/10.1029/2011JB008973>
- Chester, F. M., & Chester, J. S. (2000). Stress and deformation along wavy frictional faults. *Journal of Geophysical Research*, 105(B10), 23,421–23,430.
- Cocco, M., & Rice, J. R. (2002). Pore pressure and poroelasticity effects in coulomb stress analysis of earthquake interactions. *Journal of Geophysical Research*, 107(B2), 2030.
- Dalguer, L., Irikura, K., & Riera, J. (2003). Simulation of tensile crack generation by three-dimensional dynamic shear rupture propagation during an earthquake. *Journal of Geophysical Research*, 108, 2144. <https://doi.org/10.1029/2001JB001738>
- Daub, E. G., & Carlson, J. M. (2008). A constitutive model for fault gouge deformation in dynamic rupture simulations. *Journal of Geophysical Research*, 113, B12309. <https://doi.org/10.1029/2007JB005377>
- Daub, E. G., & Carlson, J. M. (2010). Friction, fracture, and earthquakes. *Annual Review of Condensed Matter Physics*, 1(1), 397–418.
- Daub, E. G., Manning, M. L., & Carlson, J. M. (2010). Pulse-like, crack-like, and supershear earthquake ruptures with shear strain localization. *Journal of Geophysical Research*, 115, B05311. <https://doi.org/10.1029/2009JB006388>
- Day, S. M. (1982). Three-dimensional finite difference simulation of fault dynamics: Rectangular faults with fixed rupture velocity. *Bulletin of the Seismological Society of America*, 72(3), 705–727.
- Di Toro, G., Goldsby, D. L., & Tullis, T. E. (2004). Friction falls towards zero in quartz rock as slip velocity approaches seismic rates. *Nature*, 427(6973), 436.
- Di Toro, G., Han, R., Hirose, T., De Paola, N., Nielsen, S., Mizoguchi, K., et al. (2011). Fault lubrication during earthquakes. *Nature*, 471(7339), 494–498.
- Dieterich, J. H. (1979). Modeling of rock friction: 1. Experimental results and constitutive equations. *Journal of Geophysical Research*, 84(B5), 2161–2168.
- Dieterich, J. (1994). A constitutive law for rate of earthquake production and its application to earthquake clustering. *Journal of Geophysical Research*, 99(B2), 2601–2618.
- Dieterich, J. H., & Smith, D. E. (2009). Nonplanar faults: Mechanics of slip and off-fault damage. *Pure and Applied Geophysics*, 166(10–11), 1799–1815.
- Dunham, E. M., & Archuleta, R. J. (2005). Near-source ground motion from steady state dynamic rupture pulses. *Geophysical Research Letters*, 32, L03302. <https://doi.org/10.1029/2004GL021793>
- Dunham, E. M., Belanger, D., Cong, L., & Kozdon, J. E. (2011a). Earthquake ruptures with strongly rate-weakening friction and off-fault plasticity, part 2: Nonplanar faults. *Bulletin of the Seismological Society of America*, 101(5), 2308–2322.
- Dunham, E. M., Belanger, D., Cong, L., & Kozdon, J. E. (2011b). Earthquake ruptures with strongly rate-weakening friction and off-fault plasticity, part 1: Planar faults. *Bulletin of the Seismological Society of America*, 101(5), 2296–2307.
- Ekström, G., Nettles, M., & Dziewoński, A. (2012). The global CMT project 2004–2010: Centroid-moment tensors for 13,017 earthquakes. *Physics of the Earth and Planetary Interiors*, 200, 1–9.
- El Hariri, M., Abercrombie, R. E., Rowe, C. A., & Do Nascimento, A. F. (2010). The role of fluids in triggering earthquakes: Observations from reservoir induced seismicity in Brazil. *Geophysical Journal International*, 181(3), 1566–1574.
- Erlingsson, S., & Einarsson, P. (1989). Distance changes in the south Iceland seismic zone 1977–1984. *Jökull*, 39, 32–40.
- Eshelby, J. D. (1957). The determination of the elastic field of an ellipsoidal inclusion, and related problems. *Proceedings of the Royal Society of London A*, 241(1226), 376–396.
- Fang, Z., & Dunham, E. M. (2013). Additional shear resistance from fault roughness and stress levels on geometrically complex faults. *Journal of Geophysical Research: Solid Earth*, 118, 3642–3654.
- Faulkner, D., Lewis, A., & Rutter, E. (2003). On the internal structure and mechanics of large strike-slip fault zones: Field observations of the carboneras fault in southeastern Spain. *Tectonophysics*, 367(3–4), 235–251.
- Felzer, K. R., & Brodsky, E. E. (2006). Decay of aftershock density with distance indicates triggering by dynamic stress. *Nature*, 441(7094), 735.
- Freed, A. M. (2005). Earthquake triggering by static, dynamic, and postseismic stress transfer. *Annual Review of Earth and Planetary Sciences*, 33, 335–367.
- Gabriel, A.-A., Ampuero, J.-P., Dalguer, L., & Mai, P. M. (2013). Source properties of dynamic rupture pulses with off-fault plasticity. *Journal of Geophysical Research: Solid Earth*, 118, 4117–4126. <https://doi.org/10.1002/jgrb.50213>
- Gardner, J., & Knopoff, L. (1974). Is the sequence of earthquakes in Southern California, with aftershocks removed, Poissonian? *Bulletin of the Seismological Society of America*, 64(5), 1363–1367.
- Goldsby, D. L., & Tullis, T. E. (2002). Low frictional strength of quartz rocks at subseismic slip rates. *Geophysical Research Letters*, 29(17), 1844. <https://doi.org/10.1029/2002GL015240>
- Goldsby, D. L., & Tullis, T. E. (2011). Flash heating leads to low frictional strength of crustal rocks at earthquake slip rates. *Science*, 334(6053), 216–218.

- Gomberg, J., Bodin, P., & Reasenberg, P. A. (2003). Observing earthquakes triggered in the near field by dynamic deformations. *Bulletin of the Seismological Society of America*, 93(1), 118–138.
- Gupta, H. K. (2002). A review of recent studies of triggered earthquakes by artificial water reservoirs with special emphasis on earthquakes in Koyna, India. *Earth-Science Reviews*, 58(3-4), 279–310.
- Gutenberg, B., & Richter, C. F. (1944). Frequency of earthquakes in California. *Bulletin of the Seismological Society of America*, 34(4), 185–188.
- Hainzl, S. (2004). Seismicity patterns of earthquake swarms due to fluid intrusion and stress triggering. *Geophysical Journal International*, 159(3), 1090–1096.
- Hainzl, S., Zoeller, G., & Wang, R. (2010). Impact of the receiver fault distribution on aftershock activity. *Journal of Geophysical Research*, 115, B05315. <https://doi.org/10.1029/2008JB006224>
- Hanks, T. C. (1977). Earthquake stress drops, ambient tectonic stresses and stresses that drive plate motions. In M. Wyss (Ed.), *Stress in the Earth* Vol. 115, pp. 441–458. Birkhäuser, Basel: Springer.
- Hanks, T. C. (1992). Small earthquakes, tectonic forces. *Science*, 256(5062), 1430–1432.
- Hanks, T. C., & Bakun, W. H. (2002). A bilinear source-scaling model for M-log A observations of continental earthquakes. *Bulletin of the Seismological Society of America*, 92(5), 1841–1846.
- Hanks, T. C., & Bakun, W. H. (2008). M-log A observations for recent large earthquakes. *Bulletin of the Seismological Society of America*, 98(1), 490–494.
- Hardebeck, J. (2010). Aftershocks are well aligned with the background stress field, contradicting the hypothesis of highly heterogeneous crustal stress. *Journal of Geophysical Research*, 115, B12308. <https://doi.org/10.1029/2010JB007586>
- Hardebeck, J. L. (2015). Comment on models of stochastic, spatially varying stress in the crust compatible with focal-mechanism data, and how stress inversions can be biased toward the stress rate by Deborah Elaine Smith and Thomas H. Heaton, *Bulletin of the Seismological Society of America*, 105(1), 447–451.
- Hardebeck, J. L., Nazareth, J. J., & Hauksson, E. (1998). The static stress change triggering model: Constraints from two Southern California aftershock sequences. *Journal of Geophysical Research*, 103(B10), 24,427–24,437.
- Harris, R. A. (2004). Numerical simulations of large earthquakes: Dynamic rupture propagation on heterogeneous faults. In A. Donnellan, P. Mora, M. Matsuzawa, & X. Yin (Eds.), *Computational Earthquake Science Part II* (Vol. 161, pp. 2171–2181). Birkhäuser, Basel: Springer.
- Harris, R., Barall, M., Aagaard, B., Ma, S., Roten, D., Olsen, K., et al. (2018). A suite of exercises for verifying dynamic earthquake rupture codes. *Seismological Research Letters*, 89(3), 1146–1162.
- Harris, R., Barall, M., & Archuleta, R. (2009). The SCEC/USGS dynamic earthquake rupture code verification exercise. *Seismological Research Letters*, 80(1), 119–126.
- Harris, R. A., & Day, S. M. (1997). Effects of a low-velocity zone on a dynamic rupture. *Bulletin of the Seismological Society of America*, 87(5), 1267–1280.
- Hauksson, E. (2010). Spatial separation of large earthquakes, aftershocks, and background seismicity: Analysis of interseismic and coseismic seismicity patterns in southern California. In M. K. Savage, D. A. Rhoades, E. G. C. Smith, M. C. Gerstenberger, & D. Vere-Jones (Eds.), *Seismogenesis and Earthquake Forecasting: The Frank Evison Volume II* (pp. 125–143). Birkhäuser, Basel: Springer.
- Hauksson, E. (2011). Crustal geophysics and seismicity in southern California. *Geophysical Journal International*, 186(1), 82–98.
- Helmstetter, A., Kagan, Y. Y., & Jackson, D. D. (2005). Importance of small earthquakes for stress transfers and earthquake triggering. *Journal of Geophysical Research*, 110, B05S08. <https://doi.org/10.1029/2004JB003286>
- Hill, D. P., Pollitz, F., & Newhall, C. (2002). Earthquake-volcano interactions. *Physics Today*, 55(11), 41–47.
- Hill, D., Reasenberg, P. A., Michael, A., Arabaz, W. J., Beroza, G., Brumbaugh, D., et al. (1993). Seismicity remotely triggered by the magnitude 7.3 Landers, California, earthquake. *Science*, 260(5114), 1617–1623.
- Hirose, T., & Bystricky, M. (2007). Extreme dynamic weakening of faults during dehydration by coseismic shear heating. *Geophysical Research Letters*, 34, 14311. <https://doi.org/10.1029/2007GL030049>
- Hirose, T., & Shimamoto, T. (2005). Growth of molten zone as a mechanism of slip weakening of simulated faults in gabbro during frictional melting. *Journal of Geophysical Research*, 110, B05202. <https://doi.org/10.1029/2004JB003207>
- Ida, Y. (1972). Cohesive force across the tip of a longitudinal-shear crack and Griffith's specific surface energy. *Journal of Geophysical Research*, 77(20), 3796–3805.
- Ionescu, I. R., & Campillo, M. (1999). Influence of the shape of the friction law and fault finiteness on the duration of initiation. *Journal of Geophysical Research*, 104(B2), 3013–3024.
- Kagan, Y. Y. (1994). Distribution of incremental static stress caused by earthquakes. *Nonlinear Processes in Geophysics*, 1(2/3), 172–181.
- Kilb, D., Ellis, M., Gomberg, J., & Davis, S. (1997). On the origin of diverse aftershock mechanisms following the 1989 Loma Prieta earthquake. *Geophysical Journal International*, 128(3), 557–570.
- King, G. C., Hubert-Ferrari, A., Nalbant, S. S., Meyer, B., Armijo, R., & Bowman, D. (2001). Coulomb interactions and the 17 August 1999 Izmit, Turkey earthquake. *Comptes Rendus de l'Académie des Sciences-Series IIA-Earth and Planetary Science*, 333(9), 557–569.
- King, G. C., Stein, R. S., & Lin, J. (1994). Static stress changes and the triggering of earthquakes. *Bulletin of the Seismological Society of America*, 84(3), 935–953.
- Kozdon, J. E., Dunham, E. M., & Nordström, J. (2012). Interaction of waves with frictional interfaces using summation-by-parts difference operators: Weak enforcement of nonlinear boundary conditions. *Journal of Scientific Computing*, 50(2), 341–367.
- Kozdon, J. E., Dunham, E. M., & Nordström, J. (2013). Simulation of dynamic earthquake ruptures in complex geometries using high-order finite difference methods. *Journal of Scientific Computing*, 55(1), 92–124.
- Lee, J.-J., & Brunn, R. L. (1996). Structural anisotropy of normal fault surfaces. *Journal of Structural Geology*, 18(8), 1043–1059.
- Lin, J., & Stein, R. S. (2004). Stress triggering in thrust and subduction earthquakes and stress interaction between the southern San Andreas and nearby thrust and strike-slip faults. *Journal of Geophysical Research*, 109, B02303. <https://doi.org/10.1029/2003JB002607>
- Liseikin, V. D. (2009). *Grid generation methods*. Berlin: Springer Science & Business Media.
- Lohman, R. B., & McGuire, J. J. (2007). Earthquake swarms driven by aseismic creep in the Salton Trough, California. *Journal of Geophysical Research*, 112, B04405. <https://doi.org/10.1029/2006JB004596>
- Mai, P. M., & Thingbaijam, K. (2014). Srcmod: An online database of finite-fault rupture models. *Seismological Research Letters*, 85(6), 1348–1357.
- Mallman, E. P., & Parsons, T. (2008). A global search for stress shadows. *Journal of Geophysical Research*, 113, B12304. <https://doi.org/10.1029/2007JB005336>
- Marsan, D. (2005). The role of small earthquakes in redistributing crustal elastic stress. *Geophysical Journal International*, 163(1), 141–151.

- Meier, M.-A., Werner, M., Woessner, J., & Wiemer, S. (2014). A search for evidence of secondary static stress triggering during the 1992 Mw7.3 Landers, California, earthquake sequence. *Journal of Geophysical Research: Solid Earth*, 119, 3354–3370. <https://doi.org/10.1002/2013JB010385>
- Myers, R., & Aydin, A. (2004). The evolution of faults formed by shearing across joint zones in sandstone. *Journal of Structural Geology*, 26(5), 947–966.
- Nandan, S., Ouillon, G., Woessner, J., Sornette, D., & Wiemer, S. (2016). Systematic assessment of the static stress triggering hypothesis using interearthquake time statistics. *Journal of Geophysical Research: Solid Earth*, 121, 1890–1909. <https://doi.org/10.1002/2015JB012212>
- Nur, A., & Booker, J. R. (1972). Aftershocks caused by pore fluid flow? *Science*, 175(4024), 885–887.
- Okubo, P. G., & Aki, K. (1987). Fractal geometry in the San Andreas fault system. *Journal of Geophysical Research*, 92(B1), 345–355.
- Parsons, T., Stein, R. S., Simpson, R. W., & Reasenberg, P. A. (1999). Stress sensitivity of fault seismicity: A comparison between limited-offset oblique and major strike-slip faults. *Journal of Geophysical Research*, 104(B9), 20,183–20,202.
- Pedersen, R., Jónsson, S., Árnadóttir, T., Sigmundsson, F., & Feigl, K. L. (2003). Fault slip distribution of two June 2000 Mw 6.5 earthquakes in South Iceland estimated from joint inversion of InSAR and GPS measurements. *Earth and Planetary Science Letters*, 213(3-4), 487–502.
- Perfettini, H., & Avouac, J.-P. (2004). Postseismic relaxation driven by brittle creep: A possible mechanism to reconcile geodetic measurements and the decay rate of aftershocks, application to the Chi-Chi earthquake, Taiwan. *Journal of Geophysical Research*, 109, B02304. <https://doi.org/10.1029/2003JB002488>
- Power, W., & Tullis, T. (1995). Review of the fractal character of natural fault surfaces with implications for friction and the evolution of fault zones. In C. C. Barton & P. R. La Pointe (Eds.), *Fractals in the Earth Sciences* (Chap. 5, pp. 89–105). New York: Plenum Press.
- Power, W., Tullis, T., Brown, S., Boitnott, G., & Scholz, C. (1987). Roughness of natural fault surfaces. *Geophysical Research Letters*, 14(1), 29–32.
- Power, W. L., Tullis, T. E., & Weeks, J. D. (1988). Roughness and wear during brittle faulting. *Journal of Geophysical Research*, 93(B12), 15,268–15,278.
- Powers, P. M., & Jordan, T. H. (2010). Distribution of seismicity across strike-slip faults in California. *Journal of Geophysical Research*, 115, B05305. <https://doi.org/10.1029/2008JB006234>
- Renard, F., Voisin, C., Marsan, D., & Schmittbuhl, J. (2006). High resolution three dimensional laser scanner measurements of a strike-slip fault quantify its morphological anisotropy at all scales. *Geophysical Research Letters*, 33, L04305. <https://doi.org/10.1029/2005GL025038>
- Rice, J. R., Sammis, C. G., & Parsons, R. (2005). Off-fault secondary failure induced by a dynamic slip pulse. *Bulletin of the Seismological Society of America*, 95(1), 109–134.
- Rubin, A. M., & Ampuero, J.-P. (2007). Aftershock asymmetry on a bimaterial interface. *Journal of Geophysical Research*, 112, B05307. <https://doi.org/10.1029/2006JB004337>
- Rubin, A. M., & Gillard, D. (2000). Aftershock asymmetry/rupture directivity among central San Andreas fault microearthquakes. *Journal of Geophysical Research*, 105(B8), 19,095–19,109.
- Ruina, A. (1983). Slip instability and state variable friction laws. *Journal of Geophysical Research*, 88(B12), 10,359–10,370.
- Russ, J. C. (1994). *Fractal Surfaces*. New York: Plenum.
- Sagy, A., Brodsky, E. E., & Axen, G. J. (2007). Evolution of fault-surface roughness with slip. *Geology*, 35(3), 283–286.
- Salichon, J., Lundgren, P., Delouis, B., & Giardini, D. (2004). Slip history of the 16 October 1999 Mw 7.1 Hector Mine earthquake (California) from the inversion of InSAR, GPS, and teleseismic data. *Bulletin of the Seismological Society of America*, 94(6), 2015–2027.
- Schmedes, J., Archuleta, R. J., & Lavallée, D. (2010). Correlation of earthquake source parameters inferred from dynamic rupture simulations. *Journal of Geophysical Research*, 115, B03304. <https://doi.org/10.1029/2009JB006689>
- Scholz, C. H. (1982). Scaling laws for large earthquakes: Consequences for physical models. *Bulletin of the Seismological Society of America*, 72(1), 1–14.
- Segou, M., & Parsons, T. (2014). The stress shadow problem in physics-based aftershock forecasting: Does incorporation of secondary stress changes help? *Geophysical Research Letters*, 41, 3810–3817. <https://doi.org/10.1002/2013GL058744>
- Shaw, B. E., Richards-Dinger, K., & Dieterich, J. H. (2015). Deterministic model of earthquake clustering shows reduced stress drops for nearby aftershocks. *Geophysical Research Letters*, 42, 9231–9238. <https://doi.org/10.1002/2015GL066082>
- Shearer, P., Hauksson, E., & Lin, G. (2005). Southern California hypocenter relocation with waveform cross-correlation, part 2: Results using source-specific station terms and cluster analysis. *Bulletin of the Seismological Society of America*, 95(3), 904–915.
- Shi, Z., & Ben-Zion, Y. (2006). Dynamic rupture on a bimaterial interface governed by slip-weakening friction. *Geophysical Journal International*, 165(2), 469–484.
- Shi, Z., & Day, S. M. (2013). Rupture dynamics and ground motion from three dimensional rough-fault simulations. *Journal of Geophysical Research: Solid Earth*, 118, 1122–1141. <https://doi.org/10.1002/jgrb.50094>
- Skempton, A. (1954). The pore-pressure coefficients a and b. *Geotechnique*, 4(4), 143–147.
- Smith, D. E., & Dieterich, J. H. (2010). Aftershock sequences modeled with 3-D stress heterogeneity and rate-state seismicity equations: Implications for crustal stress estimation. In M. K. Savage, D. A. Rhoades, D. A. Rhoades, E. G. C. Smith, M. C. Gerstenberger & D. Vere-Jones (Eds.), *Seismogenesis and Earthquake Forecasting: The Frank Elsworth Volume II* (pp. 213–231). Basel: Springer.
- Smith, D. E., & Heaton, T. H. (2011). Models of stochastic, spatially varying stress in the crust compatible with focal-mechanism data, and how stress inversions can be biased toward the stress rate. *Bulletin of the Seismological Society of America*, 101(3), 1396–1421.
- Steacy, S., Marsan, D., Nalbant, S. S., & McCloskey, J. (2004). Sensitivity of static stress calculations to the earthquake slip distribution. *Journal of Geophysical Research*, 109, B04303. <https://doi.org/10.1029/2002JB002365>
- Thatcher, W., & Hanks, T. C. (1973). Source parameters of Southern California earthquakes. *Journal of Geophysical Research*, 78(35), 8547–8576.
- Tinti, E., Bazzarri, A., & Cocco, M. (2005). Modeling the dynamic rupture propagation on heterogeneous faults with rate-and state-dependent friction. *Annals of Geophysics*, 48, 327–345.
- Toda, S., Lin, J., Meghraoui, M., & Stein, R. S. (2008). 12 May 2008 M= 7.9 Wenchuan, China, earthquake calculated to increase failure stress and seismicity rate on three major fault systems. *Geophysical Research Letters*, 35, L17305. <https://doi.org/10.1029/2008GL034903>
- Toda, S., Stein, R. S., Beroza, G. C., & Marsan, D. (2012). Aftershocks halted by static stress shadows. *Nature Geoscience*, 5(6), 410.
- Toda, S., Stein, R. S., Reasenberg, P. A., Dieterich, J. H., & Yoshida, A. (1998). Stress transferred by the 1995 Mw = 6.9 Kobe, Japan, shock: Effect on aftershocks and future earthquake probabilities. *Journal of Geophysical Research*, 103(B10), 24,543–24,565.
- Tsutsumi, A., & Shimamoto, T. (1997). High-velocity frictional properties of gabbro. *Geophysical Research Letters*, 24(6), 699–702.
- Vidale, J. E., Boyle, K. L., & Shearer, P. M. (2006). Crustal earthquake bursts in California and Japan: Their patterns and relation to volcanoes. *Geophysical research letters*, 33, L20313. <https://doi.org/10.1029/2006GL027723>

- Vidale, J. E., & Shearer, P. M. (2006). A survey of 71 earthquake bursts across Southern California: Exploring the role of pore fluid pressure fluctuations and aseismic slip as drivers. *Journal of Geophysical Research*, 111, B05312. <https://doi.org/10.1029/2005JB004034>
- Waite, G. P., & Smith, R. B. (2002). Seismic evidence for fluid migration accompanying subsidence of the Yellowstone caldera. *Journal of Geophysical Research*, 107(B9), 2177.
- Wald, D. J., & Heaton, T. H. (1994). Spatial and temporal distribution of slip for the 1992 Landers, California, earthquake. *Bulletin of the Seismological Society of America*, 84(3), 668–691.
- Walshauer, F., & Schaff, D. P. (2008). Large-scale relocation of two decades of Northern California seismicity using cross-correlation and double-difference methods. *Journal of Geophysical Research*, 113, B08311. <https://doi.org/10.1029/2007JB005479>
- Wells, D. L., & Coppersmith, K. J. (1994). New empirical relationships among magnitude, rupture length, rupture width, rupture area, and surface displacement. *Bulletin of the Seismological Society of America*, 84(4), 974–1002.
- Wesnousky, S. G. (2008). Displacement and geometrical characteristics of earthquake surface ruptures: Issues and implications for seismic-hazard analysis and the process of earthquake rupture. *Bulletin of the Seismological Society of America*, 98(4), 1609–1632.
- Zeng, Y., & Anderson, J. (2000). Evaluation of numerical procedures for simulating near-fault long-period ground motions using Zeng method, report 2000/01 to the PEER utilities program.